Separative magnetization transport: theory, model, and experiment

Rico A. R. Picone

A dissertation
submitted in partial fulfillment of the
requirements for the degree of

Doctor of Philosophy

University of Washington

2014

Reading Committee:

Joseph L. Garbini, Chair

John A. Sidles

Santosh Devasia

Program Authorized to Offer Degree:
University of Washington Department of Mechanical Engineering

University of Washington

Abstract

Separative magnetization transport: theory, model, and experiment

Rico A. R. Picone

Chair of the Supervisory Committee:
Professor Joseph L. Garbini
Mechanical Engineering

We present a theoretical framework for modeling the transport of any number of globally conserved quantities, in any spatial configuration, and apply it to obtain a model of magnetization transport for spin-systems with two spin-species. The framework allows an entropy function to define a model that explicitly respects the laws of thermodynamics. A one-species model is derived as a special case. In the high spin-temperature (linear) limit, this model is shown to be equivalent to the model of nuclear spin transport of Genack and Redfield (Genack and Redfield, 1975). The two-species model is novel in that it describes systems of two spin-species and systems with large polarization. It is explored numerically and shown to be consistent with experimental results, which are also presented, but are insufficient to validate the model. This is followed by a numerical exploration of a potential experiment that could validate the model. Analytic, steady state solutions for the one- and two-species models are derived. The separative quality of transport is quantified by two figures of merit: one static and the other dynamic. The theoretical framework, two-species model, and experimental results provide a foundation for further study of separative magnetization transport (SMT), and in particular the study of harnessing it to induce hyperpolarization by optimizing the presented figures of merit.

Table of Contents

Page

List of Figures

Acknowledgments

I would like to acknowledge John Marohn and Dan Rugar for a number of fruitful discussions regarding the experiment and the applications of separative magnetization transport. John Lee wrote the beautiful work *Introduction to Smooth Manifolds*[1] which guided me through much of the mathematics; and when I lost my way, his personal guidance. John Sidles was the inspiration of the entire field in which this work lies, and without his untiring devotion, this dissertation would never have gotten off the ground. Without Joseph Garbini, it would never have landed; and I would not have learned (by his example) what it means to be a world-class engineer and an educator.

---

[1] See Lee (2012).

Dedication

Now this is not the end.
It is not even the beginning of the end.
But it is, perhaps, the end of the beginning.

Winston Churchill
London, 10 November 1942
(The Churchill Centre)

For John Sidles and Joe Garbini — the fathers of quantum systems engineering.

Chapter 1

Introduction

Magnetization transport for a spin-system in a spatially varying magnetic field has been studied theoretically (Genack and Redfield, 1975) and experimentally (Eberhardt et al., 2007; Budakian et al., 2004). Thus far, neither a multiple spin-species model, nor a model (of one- or two-species) that is valid for large polarization has been published.[1] We propose such models, and examine their specifically *separative* character, with emphasis on the possibility of harnessing separative magnetization transport (SMT) for the *hyperpolarization* of nuclear magnetization. With recent significant enhancements of the technique of *dynamic nuclear polarization* (DNP) (Ni et al., 2013; Krummenacker et al., 2012; Abragam and Goldman, 1978), which has been shown to achieve significant *hyperpolarization*, and with the current study of the possibility of hyperpolarizing samples through SMT, models that can describe the high-polarization regime in a spatially varying magnetic field are needed. Hyperpolarization would boost the signal in any device measuring magnetic resonance, such as the magnetic resonance force microscopy (MRFM) apparatus with which the experiment of Appendix A was performed.

Early rudimentary analysis of SMT predicted significant hyperpolarization that was not observed in experiment, as described in Appendix A (Measuring separative magnetization transport). The primary impetus for the detailed theory and model presented in Chapter 2 (Framework for transport analysis) and Chapter 3 (Modeling magnetization transport: two spin-species) was to understand this experiment and lay the groundwork for further exploration of SMT.

The theory and model of Chapter 2 and Chapter 3 describe, as a special case, the dynamics of a one-species spin system, as derived in Chapter 4 (Modeling magnetization transport: one spin-species). The high-temperature one-species models of magnetization transport, such as that of Genack and Redfield, do not apply for systems with high-polarization. In the high-temperature limit of the one-species model of Chapter 4, we find congruence with the model of Genack and

---

[1] The article Picone et al. (forthcoming) proposes the framework of Chapter 2 and a one spin-species model. A portion of what follows is contained in that publication.

Redfield, which we take to be a validation of the proposed entropy function of Chapter 3.

A numerical study of the two-species model is undertaken in Chapter 5 (Numerical investigations of the two spin-species model). This includes an investigation of the performed experiment that explains its results. However, its (null) results were insufficiently descriptive to validate the model. The dynamics of the two-species system are further explored by investigating a proposed experiment that could be performed to validate the model, which predicts a doubling of nuclear polarization in this case. This is not believed to be an experiment with maximal hyperpolarization, but one that is straightforward to instantiate.

Chapter 2

Framework for transport analysis

In this chapter, a framework for transport analysis is presented that respects the four laws of thermodynamics, that can describe various spatial geometries, and that can be extended to any number of conserved quantities.

We begin with a discussion of the two fundamental processes of transport: diffusion and separation.

2.1 Transport: diffusion & separation

The well-known diffusion equation for some function ρ and positive scalar coefficient Γ is

$$\partial_t \rho = \Gamma \nabla^2 \rho. \tag{2.1}$$

Its key feature is that local concentrations of ρ are diminished, leading to uniform distributions.

However, another process is observed in, for example, chromatography, field-flow fractionation Giddings (1991), and isotope separation. These technologies exhibit an effect called *separation* that concentrates ρ, and is thus the opposite of diffusion.

According to Giddings, with regard to mass transport,

> Separation is the art and science of maximizing separative transport relative to dispersive transport.[1]

By "dispersive transport," Giddings means what we have called "diffusion"; by "separative transport," he means a process in which the concentration of some distributed quantity is achieved. We adopt the language of Giddings for the dynamics of magnetization: *transport* is the general term, including both diffusion and separation.

---

[1] See Giddings (1991), p. 10.

Equation 2.1 has no provision for separation. The models of mass transport are not immediately applicable to magnetization transport because clear analogs are not available for some features (e.g. there is no magnetization analog for the gravitational gradient in distillation towers).[2] Moreover, the mass transport models are not dynamic. We present a framework for transport analysis and subsequent dynamic models that include both diffusion and separation.

2.2 Framework for transport analysis

We will proceed in the coordinate-free language of differential geometry, which allows the laws of thermodynamics to be respected explicitly, regardless of spatial geometry or the number of conserved quantities.

What follows is a necessarily extensive list of definitions and remarks. As we will see, the mathematical rigor of these definitions will enable and greatly simplify the subsequent theoretical development.

The following definitions are the elements from which two propositions are constructed that describe a framework for transport analysis and its adherence to the laws of thermodynamics. In any specific application of the theory, defining the spatial geometry, conserved quantities, entropy function, and a space-time scale will be sufficient to construct a model of transport that respects the laws of thermodynamics from the following definitions (as detailed in Remark 2.2).

The elements of the framework are defined in the following order:

(a) the spatial manifold, metric, and coordinates;
(b) conserved quantities and their local densities;
(c) the entropy density and thermodynamic potentials;
(d) Onsager's kinetic coefficients;
(e) the current of local quantity densities;
(f) the continuity equation for local densities; and
(g) a transport rate tensor and an *ansatz* further specifying the kinetic coefficients.

Proposition 2.1 will describe how the laws of thermodynamics are satisfied in the definitions and Proposition 2.2 will assert that the definitions describe a physically valid model of transport. We begin with spatial considerations.

Definition 2.1 (spatial manifold)**.** Let $\mathcal{U}$ be a Riemannian (smooth) manifold, which represents the spatial geometry of a macroscopic thermodynamic system. We call $\mathcal{U}$ the *spatial manifold*.

For many applications, a Euclidean space[3] $\mathbb{R}^m$ is an appropriate choice for $\mathcal{U}$.

---

[2] In Section 4.4 (The Fenske equation), a connection is made between the mass transport Fenske model and the

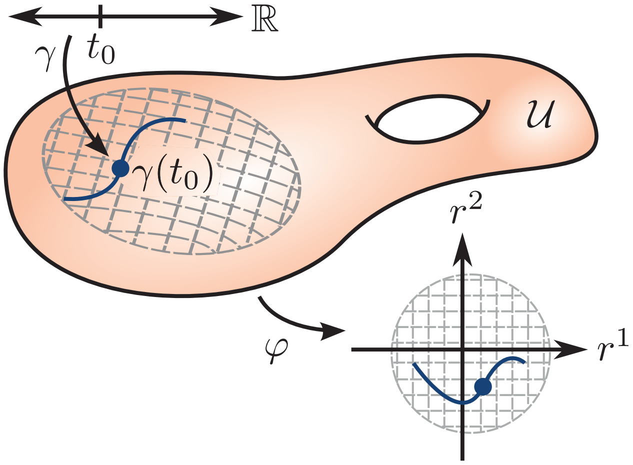

Figure 2.1: Local spatial coordinates (r^α) and coordinate map φ to $\mathbb{R}^m$ (shown here with $m = 2$). A curve $\gamma(t)$ is a map from an interval on $\mathbb{R}$ to the spatial manifold $\mathcal{U}$ and has coordinate representation $\varphi(\gamma(t))$.

Remark 2.1 (spatial coordinates). Let $\varphi : \mathcal{U} \to \mathbb{R}^m$ be some *local coordinate map*.[a] Typically, we will denote component functions of φ, defined by $\varphi(p) = \left(r^1(p), \ldots, r^m(p)\right)$ for some point $p \in \mathcal{U}$, as $(r^1, \ldots, r^m)$. These are called *local spatial coordinates*, and typically denoted (r^α). (See Figure 2.1.)

---

[a] See Lee (2012), pp. 15-16, 60-65.

By definition, the Riemannian spatial manifold $\mathcal{U}$ is endowed with a Riemannian metric, which determines the geometry of $\mathcal{U}$.

Definition 2.2 (spatial metric)**.** Let g be a *Riemannian metric*[a] on $\mathcal{U}$. We call g the *spatial metric*.

---

[a] See Lee (1997), p. 23.

In local spatial coordinates, the metric is written as

$$g = g_{\alpha\beta}\, dr^\alpha \otimes dr^\beta. \tag{2.2}$$

Definition 2.3 (conserved quantities)**.** Let $\mathbf{q} \in \mathbb{R}^n$ be the n-tuple $\mathbf{q} = (q_1, \ldots, q_n)$, where $q_i \in \mathbb{R}$ represents a *conserved quantity*.

---

steady state solution of the magnetization model.

[3] See Bullo and Lewis (2005), p. 22 and Lee (2012), p. 598.

Definition 2.4 (standard thermodynamic dual basis)**.** Let the ordered basis $(\varepsilon^1, \dots, \varepsilon^n)$ for $\mathbb{R}^n$ be

$$\varepsilon^1 = (1, 0, \dots, 0), \qquad \dots \qquad \varepsilon^n = (0, 0, \dots, 1).$$

We call this the *standard thermodynamic dual basis*,[a] and it is often denoted (ε^i).

---

[a] Although it is an uncommon practice to introduce a dual basis before a basis, we do so here because the quantities represented by the quantities $\mathbf{q}$ and $\boldsymbol{\rho}$ are more naturally—from a physical standpoint—considered dual to the potentials $\boldsymbol{\Omega}$. Yet, the quantities naturally arise first in the series of definitions.

In the standard basis, with the *Einstein summation convention*,

$$\mathbf{q} = [q_\varepsilon]_i \varepsilon^i. \tag{2.3}$$

Definition 2.5 (local quantity density)**.** Let $\mathcal{O}^*$ be the set of smooth maps from $\mathcal{U} \times \mathbb{R}$ (where $\mathbb{R}$ represents time) to $V^* \equiv \mathbb{R}^n$ (i.e. for each point in space and time we assign a vector in $\mathbb{R}^n$). Given a vector of conserved quantities $\mathbf{q}$, let $\boldsymbol{\rho} \in \mathcal{O}^*$ represent the local spatial density of each of the conserved quantities $\mathbf{q}$, such that

$$\mathbf{q} = \int_{\mathcal{U}} \boldsymbol{\rho} \; dv, \tag{2.4}$$

where dv is a volume element of $\mathcal{U}$.

In the standard thermodynamic dual basis (ε^i), we write

$$\boldsymbol{\rho} = [\rho_\varepsilon]_i \varepsilon^i, \tag{2.5}$$

where each $[\rho_\varepsilon]_i$ is a function $[\rho_\varepsilon]_i : \mathcal{U} \times \mathbb{R} \to \mathbb{R}$. The mathematical structure of $\boldsymbol{\rho}$ assigned in the definition is equivalent to a section of the product bundle $\mathcal{U} \times \mathbb{R} \times V^* \to \mathcal{U} \times \mathbb{R}$. Figure 2.2 illustrates this description, where copies of $V^* = \mathbb{R}^n$ correspond to each location in $\mathcal{U}$.

We now turn to entropic considerations.

Definition 2.6 (local entropy density)**.** Let the *local entropy volumetric density function* $s : V \to \mathbb{R}$ be a function that is nonnegative and concave.

The restriction of the local entropy density s to nonnegative functions satisfies the *third law of thermodynamics*. Moreover, we require that s be concave to allow the Legendre dual relationship that will now be introduced.

At times it is convenient to work with another set of variables called *local thermodynamic potentials*. These are significant because their spatial gradients drive the flow of $\boldsymbol{\rho}$.

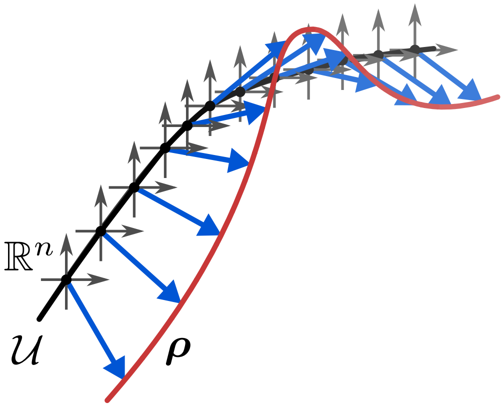

Figure 2.2: $\boldsymbol{\rho}$ considered as a time-varying section of a product bundle with (black) base $\mathcal{U}$ and (red) section $\boldsymbol{\rho}$. The (gray) vector space $V^* = \mathbb{R}^n$ is duplicated at each point on $\mathcal{U}$. Each copy of $\mathbb{R}^n$ corresponds to a (blue) arrow that represents $\boldsymbol{\rho}$ at that point in space and at some given time. In this example, $\mathcal{U}$ is one-dimensional (with curvature) and the vector space is $\mathbb{R}^2$, meaning there is a single spatial dimension and there are two conserved quantities.

$$\begin{tikzcd}
\mathbb{R} & V^* \arrow[l, "s"'] \arrow[r, "ds"] & V \\
& \mathcal{U} \times \mathbb{R} \arrow[u, "\boldsymbol{\rho}"] \arrow[ur, "\boldsymbol{\Omega}"'] &
\end{tikzcd}$$

Figure 2.3: A commutative diagram relating the spacetime manifold $\mathcal{U} \times \mathbb{R}$, to thermodynamic quantity densities $\boldsymbol{\rho} \in \mathcal{O}^*$, thermodynamic potentials $\boldsymbol{\Omega} \in \mathcal{O}$, and the entropy density function $s \in C^\infty(V^*, \mathbb{R})$.

Definition 2.7 (local thermodynamic potentials)**.** Let $\boldsymbol{\Omega} : \mathcal{U} \times \mathbb{R} \to V$ be defined by the relation

$$\boldsymbol{\Omega} = ds \circ \boldsymbol{\rho}, \tag{2.6}$$

where the exterior derivative d is taken with respect to the vector space V^*.[a] We call $\boldsymbol{\Omega}$ the *local thermodynamic potential*, and it is the Legendre transform[b] n-tuple conjugate of $\boldsymbol{\rho}$. The dual space of $\mathcal{O}^*$ is denoted $\mathcal{O}$, and so $\boldsymbol{\Omega} \in \mathcal{O}$. The duality gives the *standard thermodynamic basis* (E_i) to be such that $E_i(\varepsilon^j) = \delta^j_i$, where δ is the Kronecker-delta.

---

[a] The vector space V^* has dual space $V^{**} = V$. Therefore $\boldsymbol{\Omega} \in \mathcal{O}$ maps to vectors in V and $\boldsymbol{\rho} \in \mathcal{O}^*$ maps to covectors in V^*.

[b] For an excellent article on the Legendre transform and this duality, see Zia et al. (2009).

The standard thermodynamic basis representation of the potential is

$$\boldsymbol{\Omega} = [\Omega_E]^i E_i. \tag{2.7}$$

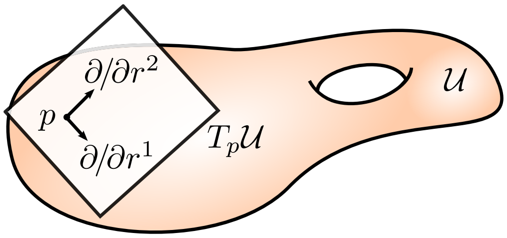

Figure 2.4: The tangent space $T_p\mathcal{U}$ at point $p \in \mathcal{U}$ with the standard basis $\partial/\partial r^\alpha|_p$.

The convention has been adopted that thermodynamic vectors are represented by uppercase symbols with upper indices on vector components (e.g. $[\Omega_E]^i$) and thermodynamic covectors are represented by lowercase symbols with lower indices on covector components (e.g. $[\rho_\varepsilon]_i$).

Commonly, inverse temperatures are the thermodynamic potentials of internal energy quantities. In this manner, other thermodynamic potentials can be considered to be analogs of inverse temperature. For instance, magnetic moment quantities have spin-temperature thermodynamic potentials. Keeping this in mind can aid the intuition that spatial gradients in $\boldsymbol{\Omega}$ drive the flow of $\boldsymbol{\rho}$, as in the familiar case of heat transfer being driven by gradients in (inverse) temperature.

We now begin to construct the current of conserved quantity densities $\mathbf{j}$. First, a discussion of spatially and thermodynamically indexed tensor structures is needed, and this requires calculus on manifolds.[4]

In order to do calculus on manifolds, the notion of a *tangent space* is required:[5] a tangent space at a point p on the spatial manifold is a vector space $T_p\mathcal{U}$ on which tangent vectors of curves through p live (see Figure 2.4). A chart that includes p provides a convenient basis for $T_p\mathcal{U}$ via its *coordinate vectors*[6] at point p, $\partial/\partial r^\alpha|_p$, where (r^α) is the local coordinate representation of $p \in \mathcal{U}$. The *tangent bundle* $T\mathcal{U}$ is the disjoint union of the tangent spaces at all points on the manifold.[7]

The *dual space of the tangent space at* p, or *cotangent space* $T_p^*\mathcal{U}$, can be given a convenient basis $dr^\alpha|_p$ by dual-mapping the tangent space basis $\partial/\partial r^\alpha|_p$ to the cotangent space. The *cotangent bundle* $T^*\mathcal{U}$ is the disjoint union of the cotangent spaces at all points on the manifold.[8].

Spatially indexed structures will be expressed in terms of the coordinate vectors $\partial/\partial r^\alpha|_p$ and coordinate covectors $dr^\alpha|_p$. Tensors that are indexed by both spatial coordinates and thermodynamic bases we call *thermometric structures*.

---

[4] See both Lee (2012) and Spivak (1965).

[5] See Lee (2012), p. 54.

[6] See Lee (2012), p. 60.

[7] See Lee (2012), pp. 65-8.

[8] See Lee (2012), pp. 272-303

The following convention for describing thermometric structures will be used. As with any tensor or tensor field, the order of their indices is merely conventional, but must be accounted. No convention is established for the ordering of the indices, but we will describe a tensor as being indexed covariantly (acting on covectors) or contravariantly (acting on vectors), first with a thermodynamic pair, say $(0, 2)$, and second with a spatial pair, say $(1, 1)$. For instance, a tensor at some point $p \in \mathcal{U}$ might be $(0, 2) \otimes (1, 1)$, which would have as its standard basis some permutation of the tensor product $dr^\alpha \otimes dr^\beta \otimes E_i \otimes \varepsilon^j$.

The convention that has been adopted is that spatial coordinate vectors $\partial/\partial r^\alpha$ and covectors dr^β are indexed by the lowercase Greek alphabet and thermodynamic basis vectors E_i and covectors ε^j are indexed by the lowercase Latin alphabet.

Definition 2.8 (Onsager kinetic coefficients)**.** Let $\hat{\mathfrak{F}}$ be defined as a positive-definite type $(0, 2) \otimes (0, 2)$ thermometric contravariant tensor field,[a] which is called *Onsager kinetic coefficients* tensor field, which serves as a thermodynamic and spatial metric.

---

[a] Note that a tensor field is a tensor bundle section.

To satisfy the *second law of thermodynamics*, $\hat{\mathfrak{F}}$ must be positive semi-definite, so Definition 2.8 satisfies the Second Law.

Typically, a contravariant tensor field is considered to assign a tensor map at each point $p \in \mathcal{U}$ from the tangent space $T_p\mathcal{U}$ to a real number. However, considering $\mathbf{\Omega}$ as a section of a fiber-bundle, it is a structure analogous to the tangent bundle $T\mathcal{U}$, and so $\hat{\mathfrak{F}}$ is indexed with both the usual cotangent local coordinate vectors dr^α and the thermodynamic dual basis (ε^i). We often use the symmetric basis for $\hat{\mathfrak{F}}$, $(\varepsilon^i \otimes dr^\alpha) \otimes (\varepsilon^j \otimes dr^\beta)$.

Definition 2.9 (current)**.** Let $\mathbf{j}$ be defined as

$$\mathbf{j} = \hat{\mathfrak{F}} \circ (d\mathbf{\Omega})^\sharp \tag{2.8}$$

where $\sharp$ is the *musical isomorphism*,[a] d is the *exterior derivative*,[b] and the symbol $\circ$ denotes a functional composition. We call $\mathbf{j}$ the *spatial transport current*.

---

[a] The musical isomorphisms are defined by the metric g as maps between the tangent bundle $T\mathcal{U}$ and the cotangent bundle $T^*\mathcal{U}$ (See Lee (2012), pp. 341-3 and Lee (1997), pp. 27-9.). The $\sharp$ operator maps spatial 1-forms to vectors.

[b] The exterior derivative is the coordinate-free generalization of the familiar differential of a function. See Lee (2012), pp. 362-72.

Equation 2.8 asserts that the current is driven by the (generalized) gradient in thermodynamic potential $\mathbf{\Omega}$, which is a multi-potential statement of the *zeroth law of thermodynamics*.

When $\mathcal{U} = \mathbb{R}^m$, as is often the case, (2.8) can be written in terms of the coordinate-free grad operator[9] as

$$\mathbf{j} = \hat{\mathfrak{F}} \circ \operatorname{grad} \boldsymbol{\Omega}. \tag{2.9}$$

With the preceding definitions, we can introduce the governing equation for $\boldsymbol{\rho}$, which is the fundamental equation of the theory of transport.

Definition 2.10 (continuity)**.** Let the *continuity equation* be defined as

$$\partial_t \boldsymbol{\rho} = d^* \mathbf{j} \tag{2.10}$$

where d^* is the *Hodge codifferential* operator.[a]

[a] The Hodge codifferential maps k-forms to $(k-1)$-forms (Lee, 2012, pp. 438-9). In (2.10) it maps a spatial 1-form to a 0-form. This is similar to the divergence operator, except that it acts on a 1-form instead of a vector.

Equation 2.10 is an expression of the global conservation of local quantities $\boldsymbol{\rho}$. It states that the local quantities $\boldsymbol{\rho}$ change with the (generalized) divergence of a current. For an energy quantity, this is the *first law of thermodynamics*.

Proposition 2.1 (laws of thermodynamics)**.** Each of the following statements is a necessary and sufficient condition for the adherence of the framework for transport analysis to the corresponding law of thermodynamics. In aggregate, then, they are necessary and sufficient conditions for adherence to all four laws of thermodynamics.

(zeroth) The current $\mathbf{j}$ satisfies the equation $\mathbf{j} = \hat{\mathfrak{F}} \circ (d\boldsymbol{\Omega})^\sharp$, as in Definition 2.9.
(first) The continuity equation is equivalent to the equation $\partial_t \boldsymbol{\rho} = d^* \mathbf{j}$, as in Definition 2.10.
(second) Onsager's kinetic coefficient tensor $\hat{\mathfrak{F}}$ is positive semi-definite, as in Definition 2.8.
(third) The local entropy density function s is non-negative, as in Definition 2.6.

Notice that, while the laws of thermodynamics have narrowed, considerably, the possible forms of the transport equation, two elements remain indefinite, although their general structures have been prescribed: the local entropy density function s and the tensor of Onsager's kinetic coefficients $\hat{\mathfrak{F}}$.

The specific form of the entropy function depends on the system, and so it is as yet necessarily unspecified. The final step, then, is to specify the form of the Onsager kinetic coefficients tensor field $\hat{\mathfrak{F}}$. Two forms are presented, the first (Definition 2.13) is quite general and is applied in Chapter 3 to model the magnetization transport of a system of two spin-species. The second (Definition 2.14) is an *ansatz* that can be used in certain applications that have a single transport rate, and is applied in Chapter 4 to model the magnetization transport of a system of one spin-species.

But, first, two more definitions are required.

---

[9] See Lee (2012), p. 368.

Definition 2.11 (covariance tensor field)**.** Let cov be defined as the negative-definite tensor field[a]

$$\mathrm{cov} = \left(\frac{\partial^2 s}{\partial \rho_i \partial \rho_j} \, E_i \otimes E_j \right)^{-1} . \tag{2.11}$$

The tensor field cov represents quantum mechanical observation processes which are related to the entropy density s by the expression.[b] We call cov the *covariance tensor field*.

---

[a] See Equation 2-11 of Onsager and Machlup (1953).

[b] This is related to the Ruppeiner metric (Ruppeiner, 1979, 1995).

This is a connection between the quantum mechanical and the macroscopic descriptions of transport. It can also be expressed in terms of a free-energy and local thermodynamic potentials, which are related to the entropy and local quantity densities by the Legendre transform.

Definition 2.12 (entropy Hessian)**.** Let $\hat{\mathfrak{G}}$ be defined as the type $(0,2) \otimes (0,2)$ thermometric contravariant tensor field

$$\hat{\mathfrak{G}} = -g \otimes \mathrm{cov}. \tag{2.12}$$

We will call $\hat{\mathfrak{G}}$ the *entropy Hessian*.

In local coordinates and the standard thermodynamic basis,

$$\hat{\mathfrak{G}} = -\left(g_{\alpha\beta} \; dr^\alpha \otimes dr^\beta \right) \otimes \left(\frac{\partial^2 s}{\partial \rho_i \partial \rho_j} \, E_i \otimes E_j \right)^{-1} . \tag{2.13}$$

A symmetric standard basis for $\hat{\mathfrak{G}}$ is $\left(\varepsilon^i \otimes dr^\alpha\right) \otimes \left(\varepsilon^j \otimes dr^\beta\right)$. $\hat{\mathfrak{G}}$ is positive-definite because g is positive-definite by its definition as a Riemannian metric and cov is by definition negative-definite.

Definition 2.13 (transport rate tensor field)**.** Let $\hat{\Gamma}$ be a $(1,1) \otimes (1,1)$ thermometric mixed tensor field called the *transport rate tensor*, which is defined by the relation

$$\hat{\mathfrak{F}} = \hat{\Gamma}(\hat{\mathfrak{G}}). \tag{2.14}$$

The transport rate tensor field $\hat{\Gamma}$ sets the space-time scales for transport. In general, there are $n^2 \times m^2$ transport space-times scales, but we often assume many fewer by symmetry and spatial isotropy.

Proposition 2.2 (framework for transport analysis)**.** Given a system of thermodynamic quantities, its covariance tensor field,[a] and its transport rate tensor — and if the system has no significant advective transport[b] — the continuity equation of Definition 2.10 and its dependent definitions describe the transport of the system over times for which global quantities $\mathbf{q}$ can be considered substantially conserved.[c]

---

[a] The covariance tensor field can be found by observation, by quantum simulation, or by an entropy density function satisfying Equation 2.11. The Legendre duality makes it equivalent to have a known, valid free energy-density function.

[b] We have not here considered the case of advective transport. For magnetization transport, this means that only solid-state magnetization samples are considered.

[c] That is, times for which Definition 2.3 holds for $\mathbf{q}$.

For certain systems (e.g. a system of spins of a single species), the following *ansatz* simplifies the analysis.

Definition 2.14 (OZ-*ansatz*)**.** Let Γ_{oz} be a real number called the *Onsager-Ziegler transport coefficient* that specifies a single space-time scale. Let the *Onsager-Ziegler ansatz* (OZ-*ansatz*) be the following relation that specifies the Onsager kinetic coefficient tensor field (Definition 2.8):

$$\hat{\mathfrak{F}}_{\text{oz}} = \Gamma_{\text{oz}}\hat{\mathfrak{G}}. \tag{2.15}$$

Equation 2.15 assumes a single space-time scale for all transport. This *ansatz* is roughly accurate in many physical systems, but we do not assert that it is generally valid. In nuclear magnetization transport, this *ansatz* is usually reasonable.[10]

Remark 2.2. Therefore, to implement the transport model for any specific system, the only elements needed are:

(a) the spatial manifold $\mathcal{U}$, metric g, and local coordinates (r^{α});
(b) the globally conserved thermodynamic quantities that define local quantity densities $\boldsymbol{\rho}$;
(c) the local entropy density function s; and
(d) the transport rate tensor $\hat{\Gamma}$.

In Chapter 3 and Chapter 4 the theoretical framework of Proposition 2.2 is developed into two magnetization transport models: one for two spin-species systems (Chapter 3) and another for one spin-species systems (Chapter 4). Both models can be derived by a process of specifying the elements described in Remark 2.2, which is described in detail in Chapter 3.

---

[10] See Genack and Redfield (1975), p. 83.

Chapter 3

Modeling magnetization transport: two spin-species

In this chapter, we construct a model of magnetization transport for a system containing both electron-spins and nuclear-spins. From the continuity equation, we develop a steady state solution and introduce two figures of merit for separative magnetization transport. The model is derived from the framework of the last chapter in one-dimension, with two spin-species, and with three conserved quantities. This development is valid for any qualifying system of two spin-species, but we choose to discuss it in terms of electron-spins and nuclear-spins. In Chapter 4 (Modeling magnetization transport: one spin-species), a one spin-species model is derived as a special case of the two-species model and shown to be equivalent, in the high spin-temperature limit, to the model of Genack and Redfield. Table 3.1 summarizes the steps for developing the two-species magnetization transport model. It shows how each element of the framework of Chapter 2 can be specified to derive the two-species model. We begin with some definitions.

Definition 3.1 (spatial manifold)**.** Let the manifold $\mathcal{U}$ be defined by $\mathcal{U} = \mathbb{R}$. We call $\mathcal{U}$ the spatial manifold.[a]

---

[a] We consider geometries with *transverse isotropy* of magnetization, external magnetic field, and sample composition; therefore, only one spatial dimension is of consequence. For this reason, although volumes are considered three-dimensional, in all other cases we consider only the single spatial dimension.

An atlas for $\mathcal{U}$ is given by the chart $\varphi : \mathcal{U} \to \mathbb{R}$, where φ is the identity, which yields the single Cartesian spatial coordinate (r) in the direction normal to the isotropic plane.

Definition 3.2 (spatial metric)**.** Let g be the (Riemannian) *Euclidean metric*, $g = dr \otimes dr$.

For the transport of two spin-species, there are three globally conserved functions on $\mathcal{U}$, so $n = 3$.

Deriving a Model of Magnetization Transport in a Magnetic Field: A Summary

Element	General Framework of Transport (Chapter 2)	1D Two-Species Magnetization Theory (Chapter 3)
spatial manifold $\mathcal{U}$	Let $\mathcal{U}$ be a Riemannian manifold (Def. 2.1) with metric g (Def. 2.2) and local coordinates (r^α) (Rem. 2.1) that represents the spatial geometry.	Let $\mathcal{U}$ be the reals (Def. 3.1, one spatial dimension), the spatial coordinate be (r), and the metric be $g = dr \otimes dr$ (Def. 3.2, Euclidean metric).
conserved quantities $\mathbf{q}$	Let the vector $\mathbf{q} \in \mathbb{R}^n$ represent conserved quantities (Def. 2.3). Let the basis (ε^i) be the standard thermodynamic dual basis for $\mathbf{q}$ (Def. 2.4).	Let $[q_\varepsilon]_1$ represent the total magnetic energy, $[q_\varepsilon]_2$ the nuclear magnetic moment, and $[q_\varepsilon]_3$ the electron magnetic moment (Def. 3.3).
quantity densities $\boldsymbol{\rho}$	Let the vector-valued function $\boldsymbol{\rho}$ represent local quantity density functions that can be integrated over $\mathcal{U}$ to obtain $\mathbf{q}$ (Def. 2.5). The function $\boldsymbol{\rho}$ inherits the basis (ε^i).	Let $[\rho_\varepsilon]_1$ represent the local energy density, $[\rho_\varepsilon]_2$ the nuclear magnetization, and $[\rho_\varepsilon]_3$ the electron magnetization (Rem. 3.1).
entropy density s	Let s be the nonnegative and concave local entropy density function of quantity densities, all of which can be expressed as basis transformations of $\boldsymbol{\rho}$.	Let s be the entropy of mixing, as described in Def. 3.4. It is expressed without explicit spatial dependence, which is convenient for the proceeding calculations.
$\boldsymbol{\rho}$-dual potential $\boldsymbol{\Omega}$	The vector of local thermodynamic potentials $\boldsymbol{\Omega}$ is the Legendre dual variable of $\boldsymbol{\rho}$ (Def. 2.7). The standard thermodynamic basis for $\boldsymbol{\Omega}$ is (E_i), where $E_i(\varepsilon^j) = \delta^j_i$.	Let $\boldsymbol{\Omega}$ be the thermodynamic potentials $[\Omega_E]^i = \partial s/\partial[\rho_\varepsilon]_i$. Henceforth, use the polarization thermodynamic basis (e_i) and dual basis (e^i) (Def. 3.7).
kinetic coef. $\hat{\mathfrak{F}}$	Let the covariance tensor field be (Def. 2.11) $\mathrm{cov} = \left(\partial^2 s/\partial\rho_i\partial\rho_j \; E_i \otimes E_j\right)^{-1}$, let the entropy Hessian be $\hat{\mathfrak{G}} = -g \otimes \mathrm{cov}$ (Def. 2.12), and let the transport rate tensor field be $\hat{\Gamma}$. Finally, define Onsager's kinetic coefficients as $\hat{\mathfrak{F}} = \hat{\Gamma}\hat{\mathfrak{G}}$ (Def. 2.13).	Compute cov, $\hat{\mathfrak{G}}$, and $\hat{\mathfrak{F}}$. The latter two are thermometric structures with four components. Determine the transport rates Γ_i from spin-system properties such as spin-species and spin-density. A spin-diffusion constant from the literature may be appropriate.
transport current $\mathbf{j}$	Let the transport current $\mathbf{j}$ be $\hat{\mathfrak{F}}$ acting on what is the gradient, in Euclidean space, of $\boldsymbol{\Omega}$ (Def. 2.9): $\mathbf{j} = \hat{\mathfrak{F}} \circ (d\boldsymbol{\Omega})^\sharp$.	Compute the current (3.13) from the thermodynamic potentials with (3.12). The steady state solution (3.18) to the continuity equation is found by setting $[j_e]_i = 0$.
governing equation of $\boldsymbol{\rho}$	Let the continuity equation, the governing equation of $\boldsymbol{\rho}$, be (Def. 2.10): $\partial_t \boldsymbol{\rho} = d^* \mathbf{j}$.	Write the continuity equation (3.15) by computing the divergence of $\mathbf{j}$, as in (3.14).

Table 3.1: *Left-to-right*: an element (left) defined in the general framework (center) is applied to specify an element of the 1D two-species magnetization model (right). *Top-to-bottom*: a summary of the derivation of the magnetization transport model.

Definition 3.3 (conserved quantities)**.** Let $\mathbf{q} \in \mathbb{R}^n$ be a vector with components: $[q_\varepsilon]_1 \in \mathbb{R}$ representing the total magnetic energy (Zeeman and dipole) in SI units J, $[q_\varepsilon]_2 \in \mathbb{R}$ representing the total magnetic moment of nuclear spins in SI units $\mathrm{A\,m^2}$, and $[q_\varepsilon]_3 \in \mathbb{R}$ representing the total magnetic moment of electron spins in SI units $\mathrm{A\,m^2}$.[a]

---

[a] The following development is valid for other two-species spin systems, when substituting the appropriate parameters (e.g. the gyromagnetic ratio).

Remark 3.1 (quantity densities). These definitions, along with the theory of Proposition 2.2, posit a temporally varying local quantity density $\boldsymbol{\rho} \in \mathcal{O}^*$, the components of which, in the standard basis, represent the energy volumetric density in SI units $\mathrm{J\,m^{-3}}$ ($[\rho_\varepsilon]_1$), the nuclear spin magnetization in SI units $\mathrm{A\,m^{-1}}$ ($[\rho_\varepsilon]_2$), and the electron spin magnetization in SI units $\mathrm{A\,m^{-1}}$ ($[\rho_\varepsilon]_3$).

3.1 Local entropy density

The local entropy density function must meet the requirements of Definition 2.6 (local entropy density). There are a number of possible forms that may be used. See Appendix B (An alternative entropy density function) for further discussion of this. Here, we choose one that is analytically tractable and predicts established results. It is based on the *entropy of mixing*, which is an entropy function that describes the mixing of several nonreactive quantities.[1]

Definition 3.4 (two-species local entropy density)**.** Let Δ_2 and Δ_3 be the temporally invariant volumetric spin densities (spins per unit volume), B be the external spatially varying magnetic field, B_d be the maximum dipole magnetic field,[a] and μ_2 and μ_3 be the magnetic moments of individual spins of each species.[b] Additionally, let the linear forms $\boldsymbol{\Psi}_1, \boldsymbol{\Psi}_2, \boldsymbol{\Psi}_3 \in \mathcal{O}$ be

$$\boldsymbol{\Psi}_1 = \frac{E_1 + B(r)\ E_2 + B(r)\ E_3}{B_d\,(|\mu_2|\Delta_2 + |\mu_3|\Delta_3)} \tag{3.1a}$$

$$\boldsymbol{\Psi}_2 = \frac{1}{\mu_2\Delta_2}\ E_2 \tag{3.1b}$$

$$\boldsymbol{\Psi}_3 = \frac{1}{\mu_3\Delta_3}\ E_3, \tag{3.1c}$$

selected to (dual) map $\boldsymbol{\rho}$ to thermodynamically significant real numbers in the interval $(-1, 1)$. Let the entropy of mixing function $\xi : (-1, 1) \to \mathbb{R}$ be

$$\xi(x) = \frac{1}{2}\ln 4 + \frac{1}{2}(x-1)\ln(1-x) - \frac{1}{2}(x+1)\ln(1+x). \tag{3.1d}$$

Then let the local entropy density $s : V^* \to \mathbb{R}$ be defined as

$$s(\boldsymbol{\rho}) = \sum_{i=1}^{n} \frac{\Delta_i}{\Delta_2}\xi(\boldsymbol{\Psi}_i(\boldsymbol{\rho})), \tag{3.2}$$

where we use $\Delta_1 = \Delta_2 + \Delta_3$.

[a] We use the estimate $B_d = \frac{\mu_0}{2\pi}(|\mu_2|\Delta_2 + |\mu_3|\Delta_3)$.

[b] For nuclear and electron spin moments, $\mu_2 = \hbar\gamma_n/2$ and $\mu_3 = -\hbar\gamma_e/2$, where $\gamma_n > 0$ and $\gamma_e > 0$ are the nuclear and electron gyromagnetic ratios.

It can be shown that (3.2) satisfies the constraints of Definition 2.6. Although this definition makes reference to the standard basis (E_i), $\boldsymbol{\Psi}_i$ can be written in any basis.

The transport has three important invariances with respect to the entropy function:

1. It is invariant to scalar addition because s enters the continuity equation only through spatial derivatives. Therefore, the maximum of entropy is inconsequential.
2. It is invariant to scalar multiplication because s enters the continuity equation twice: once in the numerator and once in the denominator. Therefore, the scaling of s is inconsequential and we choose a convenient, dimensionless function.

---

[1] See (Kardar, 2007, p. 51) and (Landau and Lifshitz, 1980, p. 282).

3. It is invariant to the choice of globally conserved quantities. Scaling $\mathbf{q}$ effectively scales s, which we have already established to be inconsequential.

3.2 Model of magnetization transport

We now define a model of magnetization transport for two spin-species. These systems do not necessarily respect the OZ-*ansatz*, so we must use the transport rate tensor field $\hat{\Gamma}$ to set the space-time scales. To remain as general as possible, the following proposition will not specify a specific form of $\hat{\Gamma}$. However, in the development that follows in Section 3.3, one is suggested.

Proposition 3.1 (model of two spin-species magnetization transport)**.** Let a magnetization system be such that the entropy of Definition 3.4 (two-species local entropy density) is valid and let the system have two spin-species such that Definition 3.3 (conserved quantities) holds. Additionally, let the system be non-advective. And let the system meet the other criteria of the framework for transport analysis of Proposition 2.2 (framework for transport analysis), using Definitions 3.1 (spatial manifold), 3.2 (spatial metric), 3.3, and 3.4 where appropriate. Then the continuity equation of Definition 2.10 and its dependent definitions describe the transport of the spin system.

3.3 Magnetization transport equation

Proposition 3.1 defines a model for a two spin-species magnetization system. In this section we explore some specific forms of this model, valid for many systems, including the system numerically and experimentally investigated in Chapter 5 (Numerical investigations of the two spin-species model) and Appendix A (Measuring separative magnetization transport).

Bases, thermodynamic potentials, and the method of derivation are discussed as a precursor to the presentation of the magnetization transport equation. A steady-state solution is developed, and the special case of thermal equilibrium is derived. Finally, two figures of merit for SMT are explored. It is important to note that in much of what follows, we assume that the spin densities Δ_i are spatially homogeneous.

3.3.1 Basis considerations

The definitions of the preceding section allow any thermodynamic basis for the local quantity density $\boldsymbol{\rho}$. In a spatially varying magnetic field, it is convenient and common practice to use a thermodynamic basis that is itself spatially varying. This is computationally advantageous and allows the continuity equation to be written in a simple component form. Two classes of basis are now defined.

Definition 3.5 (homogeneous basis)**.** Let a *homogeneous basis* be a thermodynamic ordered vector- or covector-basis that is not spatially varying.

The standard thermodynamic bases are spatially invariant, and so they are homogeneous.

Definition 3.6 (inhomogeneous basis)**.** Let an *inhomogeneous basis* be a thermodynamic ordered vector- or covector-basis that is spatially varying.

The following is a particularly convenient inhomogeneous basis.

Definition 3.7 (polarization thermodynamic covector basis)**.** Let $(e^1, \dots, e^n)$ be defined as an ordered thermodynamic covector basis by the basis transform from the standard dual basis:

$$[\rho_e]_i = [P]_i{}^j [\rho_\varepsilon]_j, \tag{3.3}$$

where P is the thermodynamic $(1,1)$ mixed tensor with matrix representation[a]

$$P = \begin{bmatrix} \dfrac{1}{B_d\left(|\mu_2|\Delta_2 + |\mu_3|\Delta_3\right)} & \dfrac{B}{B_d\left(|\mu_2|\Delta_2 + |\mu_3|\Delta_3\right)} & \dfrac{B}{B_d\left(|\mu_2|\Delta_2 + |\mu_3|\Delta_3\right)} \\ 0 & \dfrac{1}{\mu_2\Delta_2} & 0 \\ 0 & 0 & \dfrac{1}{\mu_3\Delta_3} \end{bmatrix}. \tag{3.4}$$

---

[a] For $\mu_2 = \hbar\gamma_n/2$ and $\mu_3 = -\hbar\gamma_e/2$, we can suppress the absolute values and adjust the signs accordingly.

Because $\boldsymbol{\rho}$ is a coordinate-free object, the basis vectors of (ε^i) must transform to those of (e^i) in a compensatory manner. Similarly, the polarization thermodynamic vector basis for $\boldsymbol{\Omega}$, (e_i), is easily derived. All such relations are shown in Figure 3.1.

From the relations of Figure 3.1, it can be shown that the basis covectors and vectors of the polarization basis must be spatially varying, and so it is an inhomogeneous basis. Therefore, care must be taken when computing spatial derivatives in the polarization basis.

Physical interpretations of the components of $[\rho_e]_i e^i$ ($\boldsymbol{\rho}$ in the polarization basis) are not the same as those of $[\rho_\varepsilon]_i \varepsilon^i$ ($\boldsymbol{\rho}$ in the standard basis). Both components are normalized such that they are dimensionless (their basis vectors have assimilated the units originally associated with the components). The second and third components have become the "polarization" (instead of magnetization) of each spin-species, and takes values in the interval $(-1, +1)$. The first component is a dimensionless version of the dipole-energy density (since the Zeeman energy densities of each spin-species have been subtracted from the total energy density), and it also takes values in the interval $(-1, +1)$.

$$\begin{tikzcd}
{[\rho_\varepsilon]_j} \arrow[d, "{[P]_i^{\ j}}"'] & \varepsilon^j \arrow[d, "{[P^{-\top}]^i_{\ j}}"] & \vdots & {[\Omega_E]^j} & E_j \\
{[\rho_e]_i} & e^i & \vdots & {[\Omega_e]^i} \arrow[u, "{[P^{\top}]^j_{\ i}}"] & e_i \arrow[u, "{[P^{-1}]_j^{\ i}}"']
\end{tikzcd}$$

Figure 3.1: Basis transformation relations between the standard dual basis (ε^i) and basis (E_i) and the e-dual basis and polarization basis for $\boldsymbol{\rho} = [\rho_\varepsilon]_i \varepsilon^i = [\rho_e]_i e^i$ (left) and $\boldsymbol{\Omega} = [\Omega_E]^i E_i = [\Omega_e]^i e_i$ (right). The $(1,1)$ thermodynamic tensor P of (3.4) determines the transformation.

3.3.2 The transport rate tensor field

The transport rate tensor field $\hat{\Gamma}$ has $n^2 \times m^2 = 9$ entries. We take this tensor to be diagonal, such that in the polarization thermodynamic basis, and standard spatial coordinate and time variable, it can be written

$$\hat{\Gamma} = \sum_{i=1}^{n} \sum_{j=1}^{n} [\Gamma_e]_i^j \delta_i^j \left(e^i \otimes dr\right) \otimes \left(e_j \otimes dr\right). \tag{3.5}$$

Therefore, we assign only three transport rates, which are typically written Γ_i for $i \in \{1,2,3\}$. In effect, each quantity is assigned a single rate constant.

3.3.3 Dimensionless spatial coordinates, temporal variables, and ratios

The spatial coordinate r has thus far represented a length with SI unit m and the time variable t has thus far represented a time with SI unit s. For convenience, we would like to write many of the equations that follow in dimensionless variables. Therefore, we propose the following dimensionless spatial coordinate and time variable:

$$\bar{r} = \left(\partial_r B(r)|_{r=0}/B_d\right) r \qquad \text{and} \qquad \bar{t} = \Gamma_2 \left(\partial_r B|_{r=0}/B_d\right)^2 t. \tag{3.6}$$

Functions of $\bar{t}$ and $\bar{r}$ will be denoted with a tilde above, such as $\widetilde{B}(\bar{r}) = B(r)$. We make an exception for thermodynamic quantity densities and potentials (e.g. $[\rho_e]_i$ and $[\Omega_e]^i$) in order to minimize notational clutter. When it is not clear from context, clarification will be provided in prose.

When using dimensionless space and time, dimensionless transport rates must be used. The continuity equation gives us the transformation between the transport rate tensor components in SI units and those that are dimensionless:

$$\frac{\partial \boldsymbol{\rho}/\partial t}{\partial^2 \boldsymbol{\rho}/\partial r^2} = \Gamma_2. \tag{3.7}$$

When writing the continuity equation in the dimensionless spatial coordinate and time variable

Name	Definition
Ratio of gyromagnetic ratios	$\overline{\gamma} \equiv \gamma_3/\gamma_2$
Ratio of transport coefficients	$\overline{\Gamma} \equiv \Gamma_3/\Gamma_2$
Ratio of spin densities	$\overline{\Delta} \equiv \Delta_3/\Delta_2$
Ratio of magnetic fields	$\overline{B} \equiv \partial_{\overline{r}} \widetilde{B}/B_d$
Ratio of ratios	$\overline{c} \equiv \overline{B}(1+\overline{\Delta})/(1+\overline{\gamma}\overline{\Delta})$

Table 3.2: Dimensionless ratios.

use the following transport rate tensor:

$$\hat{\Gamma} = \sum_{i=1}^{n} \sum_{j=1}^{n} \frac{[\Gamma_e]_i^j}{[\Gamma_e]_2^2} \delta_i^j \left(e^i \otimes d\overline{r}\right) \otimes \left(e_j \otimes d\overline{r}\right). \tag{3.8}$$

A number of dimensionless ratios arise in the transport equations. We define them in Table 3.2.

3.3.4 Thermodynamic potentials and spin-temperature

Definition 2.7 (local thermodynamic potentials) and Definition 3.4 (two-species local entropy density) give the polarization basis representation of the thermodynamic potential

$$[\Omega_e]^i = -\frac{\Delta_i}{\Delta_2} \operatorname{arctanh}[\rho_e]_i. \tag{3.9}$$

The units of $[\Omega_e]^i$ are dimensionless. The quantity densities $[\rho_e]_i$ take values in the interval $(-1, +1)$, and the thermodynamic potentials take corresponding values in the interval $(-\infty, +\infty)$.

Spin temperature is closely associated with $\boldsymbol{\Omega}$, which can be considered to be the inverse spin-temperature associated with each quantity $\boldsymbol{\rho}$. In the standard basis, the components of $\boldsymbol{\Omega}$ represent the inverse spin-temperatures of total energy-density ($[\Omega_E]^1$), nuclear magnetic moment ($[\Omega_E]^2$), and electron magnetic moment ($[\Omega_E]^3$). In the polarization basis, they represent the inverse spin-temperatures of the normalized dipole energy-density ($[\Omega_e]^1$), nuclear polarization ($[\Omega_e]^2$), and electron polarization ($[\Omega_e]^3$). A large polarization corresponds to a small spin temperature — which matches our expectation from the concept of spin temperature. Conversely, small potentials correspond to large spin temperatures.

From (3.9), we can solve for for the quantity densities:

$$[\rho_e]_i = -\tanh\left(\frac{\Delta_2}{\Delta_i}[\Omega_e]^i\right). \tag{3.10}$$

3.3.5 Onsager kinetic coefficient tensor field

The Onsager kinetic coefficient tensor field of Definition 2.8 can be computed using the specific definitions of entropy function, quantity densities, spatial metric, and transport rate tensor field provided in this chapter. Written as a matrix in the basis $(e^i \otimes d\bar{r}) \otimes (e^j \otimes d\bar{r})$, we obtain

$$\hat{\mathfrak{F}} = \begin{bmatrix} \frac{1+\overline{\Gamma}}{1+\overline{\Delta}}\left(1-\rho_1^2\right) & 0 & 0 \\ 0 & 1-\rho_2^2 & 0 \\ 0 & 0 & \frac{\overline{\Gamma}}{\overline{\Delta}}\left(1-\rho_3^2\right) \end{bmatrix} \tag{3.11}$$

$\hat{\mathfrak{F}}$ is positive-definite, so the transport will respect the second law of thermodynamics.

3.3.6 Spatial transport current

The spatial transport current of Definition 2.9 can be computed by acting with $\hat{\mathfrak{F}}$ of (3.11) on the tensor

$$\begin{aligned} (d\boldsymbol{\Omega})^{\sharp} = {} & \partial_{\bar{r}}[\Omega_e]^1 && e_1 \otimes \partial/\partial\bar{r} \\ & + \left(\partial_{\bar{r}}[\Omega_e]^2 + \frac{\overline{B}}{1+\overline{\gamma}\overline{\Delta}}[\Omega_e]^1\right) && e_2 \otimes \partial/\partial\bar{r} \\ & + \left(\partial_{\bar{r}}[\Omega_e]^3 - \frac{\overline{B}\overline{\gamma}\overline{\Delta}}{1+\overline{\gamma}\overline{\Delta}}[\Omega_e]^1\right) && e_3 \otimes \partial/\partial\bar{r}. \end{aligned} \tag{3.12}$$

Definition 3.8 (two-species current)**.** The *two-species transport current* is defined as

$$\begin{aligned} \mathbf{j} = {} & -\left(1+\overline{\Gamma}\right)\partial_{\bar{r}}\rho_1 && e^1 \otimes d\bar{r} \\ & + \left(-\bar{c}\left(1-\rho_2^2\right)\operatorname{arctanh}\rho_1 - \partial_{\bar{r}}\rho_2\right) && e^2 \otimes d\bar{r} \\ & + \overline{\Gamma}\left(\overline{\gamma c}\left(1-\rho_3^2\right)\operatorname{arctanh}\rho_1 - \partial_{\bar{r}}\rho_3\right) && e^3 \otimes d\bar{r}. \end{aligned} \tag{3.13}$$

3.3.7 Magnetization transport equations

The magnetization transport equation is presented in coordinates with the remaining key operation required to derive it in perhaps the most compact basis, the polarization basis.

It can be shown that the codifferential of the current is

$$\begin{aligned} d^{*}\mathbf{j} = {} & -\left(\partial_{\bar{r}}[j_e]_1 + \frac{\overline{B}\left(-[j_e]_2 + \overline{\gamma}\overline{\Delta}[j_e]_3\right)}{1+\overline{\gamma}\overline{\Delta}}\right) && e^1 \\ & - \partial_{\bar{r}}[j_e]_2 && e^2 \\ & - \partial_{\bar{r}}[j_e]_3 && e^3. \end{aligned} \tag{3.14}$$

Definition 3.9 (two-species magnetization transport equations)**.** The preferred form of the continuity equation is in the polarization basis with the dimensionless spatial coordinate and time variable, which we call the *two-species magnetization transport equations*:

$$\partial_{\bar{t}}\rho_1 = -\frac{\bar{c}^2}{1+\bar{\Delta}}\left(\left(1-\rho_2^2\right)+\overline{\Gamma\Delta}\bar{\gamma}^2\left(1-\rho_3^3\right)\right)\operatorname{arctanh}\rho_1 - \frac{\bar{c}}{1+\bar{\Delta}}\left(\partial_{\bar{r}}\rho_2 - \overline{\Gamma\Delta}\bar{\gamma}\partial_{\bar{r}}\rho_3\right) + \left(1+\bar{\Gamma}\right)\partial_{\bar{r}}^2\rho_1 \tag{3.15a}$$

$$\partial_{\bar{t}}\rho_2 = \partial_{\bar{r}}\left(\bar{c}\left(1-\rho_2^2\right)\operatorname{arctanh}\rho_1\right) + \partial_{\bar{r}}^2\rho_2 \tag{3.15b}$$

$$\partial_{\bar{t}}\rho_3 = -\bar{\Gamma}\bar{\gamma}\partial_{\bar{r}}\left(\bar{c}\left(1-\rho_3^2\right)\operatorname{arctanh}\rho_1\right) + \bar{\Gamma}\partial_{\bar{r}}^2\rho_3. \tag{3.15c}$$

If we consider only linear magnetic fields (constant field-gradients) and small dipole energy density, the magnetization transport equations become

$$\partial_{\bar{t}}\rho_1 = -\frac{\bar{c}^2}{1+\bar{\Delta}}\left(\left(1-\rho_2^2\right)+\overline{\Gamma\Delta}\bar{\gamma}^2\left(1-\rho_3^2\right)\right)\rho_1 - \frac{\bar{c}}{1+\bar{\Delta}}\left(\partial_{\bar{r}}\rho_2 - \overline{\Gamma\Delta}\bar{\gamma}\partial_{\bar{r}}\rho_3\right) + \left(1+\bar{\Gamma}\right)\partial_{\bar{r}}^2\rho_1 \tag{3.16a}$$

$$\partial_{\bar{t}}\rho_2 = \bar{c}\left(\left(1-\rho_2^2\right)\partial_{\bar{r}}\rho_1 - 2\rho_1\rho_2\partial_{\bar{r}}\rho_2\right) + \partial_{\bar{r}}^2\rho_2 \tag{3.16b}$$

$$\partial_{\bar{t}}\rho_3 = -\bar{c}\bar{\Gamma}\bar{\gamma}\left(\left(1-\rho_3^2\right)\partial_{\bar{r}}\rho_1 - 2\rho_1\rho_3\partial_{\bar{r}}\rho_3\right) + \bar{\Gamma}\partial_{\bar{r}}^2\rho_3. \tag{3.16c}$$

3.4 Steady state solution and the two-species SMT parameters

A steady state solution to Equation 3.15 is developed by setting each $[j_e]_i = 0$. This yields the system of ordinary differential equations, written in components of the polarization basis,

$$\partial_{\bar{r}}\rho_1 = 0 \tag{3.17a}$$

$$\partial_{\bar{r}}\rho_2 = -\bar{c}\left(1-\rho_2^2\right)\operatorname{arctanh}\rho_1 \tag{3.17b}$$

$$\partial_{\bar{r}}\rho_3 = \overline{\gamma c}\left(1-\rho_3^2\right)\operatorname{arctanh}\rho_1. \tag{3.17c}$$

The solution to the system in terms of unknown thermodynamic potential constants $\Omega^i(0)$ is

$$\rho_1(\bar{r}) = -\tanh\frac{\Omega^1(0)}{1+\bar{\Delta}} \tag{3.18a}$$

$$\rho_2(\bar{r}) = -\tanh\left(\Omega^2(0) - \frac{1}{1+\overline{\gamma\Delta}}\frac{\widetilde{B}(\bar{r})-\widetilde{B}(0)}{B_d}\Omega^1(0)\right) \tag{3.18b}$$

$$\rho_3(\bar{r}) = -\tanh\left(\frac{\Omega^3(0)}{\bar{\Delta}} + \frac{\bar{\gamma}}{1+\overline{\gamma\Delta}}\frac{\widetilde{B}(\bar{r})-\widetilde{B}(0)}{B_d}\Omega^1(0)\right). \tag{3.18c}$$

The corresponding thermodynamic potentials in the polarization dual basis are

$$\Omega^1(\bar{r}) = \Omega^1(0) \tag{3.19a}$$

$$\Omega^2(\bar{r}) = \Omega^2(0) - \frac{1}{1+\overline{\gamma\Delta}}\frac{\widetilde{B}(\bar{r})-\widetilde{B}(0)}{B_d}\Omega^1(0) \tag{3.19b}$$

$$\Omega^3(\bar{r}) = \Omega^3(0) + \frac{\overline{\gamma\Delta}}{1+\overline{\gamma\Delta}}\frac{\widetilde{B}(\bar{r})-\widetilde{B}(0)}{B_d}\Omega^1(0). \tag{3.19c}$$

Equation 3.18 and Equation 3.19 describe the spatial distributions of $\boldsymbol{\rho}$ and $\boldsymbol{\Omega}$ toward which magnetization transport drives the system.

3.5 Multi-spin-species Langevin paramagnetic equations

If we assume that the *Langevin paramagnetic equation*[2] describes equilibrium magnetization distributions of each spin-species individually, the unknown constants are found to be

$$\Omega^1(0) = \left(1+\overline{\gamma}\overline{\Delta}\right)\frac{\mu_2 B_d}{k_B T} = -\frac{1+\overline{\gamma}\overline{\Delta}}{\overline{\gamma}}\cdot\frac{\mu_3 B_d}{k_B T} \tag{3.20a}$$

$$\Omega^2(0) = -\frac{\mu_2\overline{B}(0)}{k_B T} \tag{3.20b}$$

$$\Omega^3(0) = -\frac{\overline{\Delta}\mu_3\overline{B}(0)}{k_B T} \tag{3.20c}$$

where T is the temperature of the sample. In this case, we can rewrite the steady state solutions as

$$\rho_1(\overline{r}) = -\tanh\left(\frac{1+\overline{\gamma}\overline{\Delta}}{1+\overline{\Delta}}\cdot\frac{\mu_2 B_d}{k_B T}\right) = \tanh\left(\frac{1+\overline{\gamma}\overline{\Delta}}{\overline{\gamma}(1+\overline{\Delta})}\cdot\frac{\mu_3 B_d}{k_B T}\right) \tag{3.21a}$$

$$\rho_2(\overline{r}) = \tanh\frac{\mu_2\widetilde{B}(\overline{r})}{k_B T} \tag{3.21b}$$

$$\rho_3(\overline{r}) = \tanh\frac{\mu_3\widetilde{B}(\overline{r})}{k_B T} \tag{3.21c}$$

and

$$\Omega^1(\overline{r}) = \left(1+\overline{\gamma}\overline{\Delta}\right)\frac{\mu_2 B_d}{k_B T} = -\frac{1+\overline{\gamma}\overline{\Delta}}{\overline{\gamma}}\cdot\frac{\mu_3 B_d}{k_B T} \tag{3.22a}$$

$$\Omega^2(\overline{r}) = -\frac{\mu_2\widetilde{B}(\overline{r})}{k_B T} \tag{3.22b}$$

$$\Omega^3(\overline{r}) = -\frac{\overline{\Delta}\mu_3\widetilde{B}(\overline{r})}{k_B T}. \tag{3.22c}$$

This result is a set of multi-spin-species Langevin paramagnetic equations. In the general steady state case, (3.18) and (3.19) are valid, yet have coefficients $\Omega^i(0)$ that may be unknown. Those constants are determined in (3.21) and (3.22) with the physical assumption (thermal equilibrium) of Langevin and Curie. Therefore, if the system is in thermal equilibrium, (3.21) and (3.22) yield its expected steady state.

---

[2] The Langevin paramagnetic equation describes the magnetization of paramagnetic moments distributed in a system with a given temperature and background magnetic field. It is derived from statistical mechanics, and is the nonlinear generalization of Curie's law, which assumes high temperatures. See (Landau and Lifshitz, 1980, p. 154) and (Kardar, 2007, p. 117).

3.6 Static and dynamic SMT figures of merit

In order to concentrate magnetization and hyperpolarize a sample, the separative aspect of magnetization transport must be understood and leveraged. In this section two figures of merit are introduced that provide researchers with metrics of separative transport.

One figure of merit of separative transport is the gradient of the steady state nuclear polarization.

Definition 3.10 (static SMT figure of merit)**.** Let $\kappa : \mathcal{U} \to \mathbb{R}$ be the *static SMT figure of merit* function

$$\kappa(\overline{r}) \equiv \partial_{\overline{r}}\rho_2(\overline{r}) = -\overline{c}\left(1-\rho_2^2\right)\operatorname{arctanh}\rho_1, \tag{3.23}$$

where ρ_i are the steady state (time-independent) components of $\boldsymbol{\rho}$ written in the polarization basis.

Separative transport of nuclear magnetization requires a gradient in its distribution, and the greater the gradient, the greater the separation. Equation 3.23 shows that, in the steady state, the greater in magnitude the product of the two terms $\overline{c} = \overline{B}(1+\overline{\Delta})/(1+\overline{\gamma}\overline{\Delta})$ and $[\rho_e]_1$ (dipole energy density), the greater the separation. When $\kappa = 0$, no separation occurs, and the flow is exclusively diffusive.

There are two prospects for increasing κ. The ratio $\overline{c}$ is composed of two terms that we will take in turn: $\overline{B}$ and $(1+\overline{\Delta})/(1+\overline{\gamma}\overline{\Delta})$. $\overline{B}$ is the dimensionless ratio

$$\overline{B} = \frac{\partial_{\overline{r}}\widetilde{B}}{B_d} = \frac{\partial_r B}{\partial_r B|_{r=0}}. \tag{3.24}$$

This ratio is always unity at $\overline{r} = 0$. However, if the field has curvature, this ratio can be greater — specifically, where the gradient of the field is *sharper* than at $\overline{r} = 0$. The ratio $(1+\overline{\Delta})/(1+\overline{\gamma}\overline{\Delta})$ approaches unity as the nuclear spin-density becomes much larger than the electron spin-density ($\overline{\Delta} \to 0$), and zero as in the opposite case. This seems to imply that the smallest possible electron spin-density is advantageous, but that ignores the effect of spin density on the dipole energy $[\rho_e]_1$, which becomes small with $\overline{\Delta}$. This implies an optimal $\overline{\Delta}$ that depends on the other factors that affect $[\rho_e]_1$.

The remaining parameter is the dipole energy $[\rho_e]_1$. In thermal equilibrium (which is *a* steady state), as we will see below, this depends on $\overline{\gamma}$, $\overline{\Delta}$, the dipole field B_d, and the temperature of the sample. B_d primarily depends on the spin-densities, and while it is larger for larger $\overline{\Delta}$ (more electron-spins), the ratio $(1+\overline{\Delta})/(1+\overline{\gamma}\overline{\Delta})$ penalizes this increase.

Another figure of merit of SMT is the non-diffusive term in Equation 3.15b.

Definition 3.11. Let $\lambda : \mathbb{R} \times \mathcal{U} \to \mathbb{R}$ be the *dynamic SMT figure of merit* function

$$\lambda(\overline{t},\overline{r}) \equiv -\partial_{\overline{r}}\left(\overline{c}\left(1-\rho_2^2\right)\operatorname{arctanh}\rho_1\right), \tag{3.25}$$

where ρ_i are the time-dependent components of $\boldsymbol{\rho}$ written in the polarization basis.

ρ_1	ρ_2	$\partial_{\bar{r}}\rho_1$	$\partial_{\bar{r}}\rho_2$	λ_1	λ_2
$-$	$+$	$+$	$+$	$+$	$+$
$+$	$-$	$+$	$+$	$+$	$+$
$+$	$+$	$+$	$-$	$+$	$+$
$-$	$-$	$+$	$-$	$+$	$+$
$+$	$+$	$-$	$+$	$-$	$-$
$-$	$-$	$-$	$+$	$-$	$-$
$-$	$+$	$-$	$-$	$-$	$-$
$+$	$-$	$-$	$-$	$-$	$-$

Table 3.3: Sign permutations of λ_2 and λ_3 that yield maximum $|\lambda|$ for the case of a uniform external magnetic field gradient $\partial_r B$.

The dynamic figure of merit is a measure of the transient separation that occurs before the steady state. By the product rule, λ is the sum of the gradient of each of the three factors in (3.25) multiplied by the other two. Due to the summation, the sign of each term is crucial. Let each term be called λ_i, where $\lambda = \sum_{i=1}^{3} \lambda_i$,

$$\lambda_1 = \left(1-\rho_2^2\right)\operatorname{arctanh}(\rho_1)\partial_{\bar{r}}\bar{c} \tag{3.26a}$$

$$= \left(1-\rho_2^2\right)\operatorname{arctanh}(\rho_1)\frac{1+\overline{\Delta}}{1+\overline{\gamma}\overline{\Delta}}\cdot\frac{B_d\partial_r^2 B}{\left(\partial_r B|_{r=0}\right)^2} \tag{3.26b}$$

$$\lambda_2 = -2\rho_2\operatorname{arctanh}(\rho_1)\bar{c}\partial_{\bar{r}}\rho_2 \tag{3.26c}$$

$$= -2\rho_2\operatorname{arctanh}(\rho_1)\frac{1+\overline{\Delta}}{1+\overline{\gamma}\overline{\Delta}}\cdot\frac{\partial_r B}{\partial_r B|_{r=0}}\partial_{\bar{r}}\rho_2 \tag{3.26d}$$

$$\lambda_3 = \frac{1-\rho_2^2}{1-\rho_1^2}\bar{c}\partial_{\bar{r}}\rho_1 \tag{3.26e}$$

$$= \frac{1-\rho_2^2}{1-\rho_1^2}\cdot\frac{1+\overline{\Delta}}{1+\overline{\gamma}\overline{\Delta}}\cdot\frac{\partial_r B}{\partial_r B|_{r=0}}\partial_{\bar{r}}\rho_1. \tag{3.26f}$$

For the case of a linear external magnetic field B, $\lambda_1 = 0$ and

$$\lambda_2 = -2\rho_2\operatorname{arctanh}(\rho_1)\frac{1+\overline{\Delta}}{1+\overline{\gamma}\overline{\Delta}}\partial_{\bar{r}}\rho_2 \tag{3.27a}$$

$$\lambda_3 = \frac{1-\rho_2^2}{1-\rho_1^2}\cdot\frac{1+\overline{\Delta}}{1+\overline{\gamma}\overline{\Delta}}\partial_{\bar{r}}\rho_1. \tag{3.27b}$$

In this case, the magnitude of λ is greatest when each factor is larger and they are of the same overall sign, which occurs in the cases shown in Table 3.3. A similar table can be constructed for the case of a field B with local curvature (in which case, λ_1 may be nonzero).

While exploring this (large) space, the magnitude of each λ_i is important, but the signs of each must be carefully considered. The optimization of this space is not analytically straightforward because each factor depends on the others through the dynamics of Equation 3.15. It requires an extensive numerical study, the beginnings of which are presented in Chapter 5 (Numerical investigations of the two spin-species model).

Although κ is simpler to analyze than λ, it is also less descriptive. Each figure of merit has its own advantages, and so both should be considered in the study of SMT. There are a number of strategies that can be used to optimize these figures of merit, and we will use a numerical approach in Chapter 5.

Chapter 4

Modeling magnetization transport: one spin-species

In this chapter, we derive a model of the magnetization transport of a spin system of one spin-species as a special case of the two-species model of Chapter 3 (Modeling magnetization transport: two spin-species). This is equivalent to beginning with the definition of an entropy function and deriving the model using the framework of Chapter 2 (Framework for transport analysis), which has been explored in Picone et al. (forthcoming) with a slightly different entropy density function. The one-species model is derived here to demonstrate that the classic results of Genack and Redfield (Section 4.3) and Fenske (Section 4.4) can be derived from it. This is a form of validation for the chosen entropy function and both the one- and two-species models. Moreover, the one-species model is of interest in itself because previously it has not appeared in a form that applied to systems with high polarization.

We begin by deriving a one-species magnetization transport equation and show its steady state solution. This model is compared to previous models and found to be equivalent in the high spin-temperature limit. Finally, the steady state solution is found to be equivalent to the mass separation equation of Fenske. In this connection to mass separation, SMT for a one-species system is discussed.

In most of what follows, we use the polarization basis of Definition 3.7 (polarization thermodynamic covector basis), the dimensionless spatial coordinate $\bar{r}$, and temporal variable $\bar{t}$ of Section 3.3.3 (Dimensionless spatial coordinates, temporal variables, and ratios).

4.1 Magnetization transport equation

We begin with the definitions of the previous chapter and show their form for modeling a system with a single spin-species. We apply the following rules for the dimensionless ratios of Table 3.2

(Dimensionless ratios.) to each structure:

$$\bar{\gamma} \to 0 \tag{4.1a}$$

$$\bar{\Gamma} \to 0 \tag{4.1b}$$

$$\bar{\Delta} \to 0 \tag{4.1c}$$

$$\bar{c} \to \bar{B}. \tag{4.1d}$$

4.1.1 The transport rate tensor field and the OZ-ansatz

The transport rate tensor field $\hat{\Gamma}$ of Definition 2.13 (transport rate tensor field) has $n^2 \times m^2 = 4$ entries. We take this tensor to be diagonal, such that in the standard thermodynamic basis, spatial coordinate, and time variable, it can be written

$$\hat{\Gamma} = \sum_{i=1}^{n} \sum_{j=1}^{n} [\Gamma_e]_i^j \delta_i^j \left(e^i \otimes dr\right) \otimes \left(e_j \otimes dr\right). \tag{4.2}$$

Therefore, we assign only two transport rates. However, we further assume that the OZ-*ansatz* of Definition 2.14 (OZ-*ansatz*) holds for the system, in effect assigning a single rate constant to both the dipole energy density and the polarization,

$$\hat{\Gamma} = \Gamma_{oz}. \tag{4.3}$$

This is a reasonable assumption for many systems (Genack and Redfield, 1975, p. 83). A diffusion coefficient may be an appropriate choice for Γ_{oz}.

We use the same dimensionless spatial coordinate $\bar{r}$ as before, and a similar dimensionless temporal variable, substituting $\Gamma_2 \to \Gamma_{oz}$,

$$\bar{t} = \Gamma_{oz} \left(\partial_r B|_{r=r_0} / B_d\right)^2 t. \tag{4.4}$$

When using dimensionless space and time, dimensionless transport rates must be used. The continuity equation gives us the transformation between the transport rate tensor components in SI units and those that are dimensionless:

$$\frac{\partial \rho / \partial t}{\partial^2 \rho / \partial r^2} = \Gamma_{oz}. \tag{4.5}$$

When writing the continuity equation in the dimensionless spatial coordinate and time variable use the following transport rate tensor:

$$\hat{\Gamma} = \frac{\Gamma_{oz}}{\Gamma_{oz}} = 1. \tag{4.6}$$

4.1.2 Thermodynamic potentials and spin-temperature

The polarization basis representation of the thermodynamic potentials of Definition 2.7 (local thermodynamic potentials) are

$$[\Omega_e]^1 = -\operatorname{arctanh}[\rho_e]_1 \qquad \text{and} \qquad [\Omega_e]^2 = -\operatorname{arctanh}[\rho_e]_2. \tag{4.7}$$

The units of $[\Omega_e]^i$ are dimensionless. The quantity densities $[\rho_e]_i$ take values in the interval $(-1, +1)$, and the thermodynamic potentials take corresponding values in the interval $(-\infty, +\infty)$.

From (4.7), we can solve for for the quantity densities:

$$[\rho_e]_1 = -\tanh[\Omega_e]^1 \qquad \text{and} \qquad [\rho_e]_2 = -\tanh[\Omega_e]^2. \tag{4.8}$$

4.1.3 Onsager kinetic coefficient tensor field

The Onsager kinetic coefficient tensor field of Equation 3.11 can be reduced and written as a matrix in the basis $(e^i \otimes d\bar{r}) \otimes (e^j \otimes d\bar{r})$, we obtain

$$\hat{\mathfrak{F}} = \begin{bmatrix} 1-\rho_1^2 & 0 \\ 0 & 1-\rho_2^2 \end{bmatrix} \tag{4.9}$$

$\hat{\mathfrak{F}}$ is positive-definite, so the transport will respect the second law of thermodynamics.

4.1.4 Spatial transport current

From Equation 3.13, we derive the current

$$\begin{aligned} \mathbf{j} = &-\partial_{\bar{r}}\rho_1 \, e^1 \otimes d\bar{r} \\ &+ \left(-\overline{B}\left(1-\rho_2^2\right)\operatorname{arctanh}\rho_1 - \partial_{\bar{r}}\rho_2\right) e^2 \otimes d\bar{r}. \end{aligned} \tag{4.10}$$

4.1.5 Magnetization transport equation

We derive the one-species magnetization transport equation from Equation 3.15 to obtain

$$\partial_{\bar{t}}\rho_1 = -\overline{B}^2\left(1-\rho_2^2\right)\operatorname{arctanh}\rho_1 - \overline{B}\partial_{\bar{r}}\rho_2 + \partial_{\bar{r}}^2\rho_1 \tag{4.11a}$$

$$\partial_{\bar{t}}\rho_2 = \partial_{\bar{r}}\left(\overline{B}\left(1-\rho_2^2\right)\operatorname{arctanh}\rho_1\right) + \partial_{\bar{r}}^2\rho_2. \tag{4.11b}$$

If we consider only linear magnetic fields (constant field-gradients) and small dipole energy density, this becomes

$$\partial_{\bar{t}}\rho_1 = -\overline{B}^2\left(1-\rho_2^2\right)\rho_1 - \overline{B}\partial_{\bar{r}}\rho_2 + \partial_{\bar{r}}^2\rho_1 \tag{4.12a}$$

$$\partial_{\bar{t}}\rho_2 = \overline{B}\left(\left(1-\rho_2^2\right)\partial_{\bar{r}}\rho_1 - 2\rho_1\rho_2\partial_{\bar{r}}\rho_2\right) + \partial_{\bar{r}}^2\rho_2. \tag{4.12b}$$

4.1.6 High spin-temperature magnetization transport equation

In the literature, high spin-temperature is often assumed (Genack and Redfield, 1975; Eberhardt et al., 2007; Ramanathan, 2008). In many applications this is sufficient. High spin-temperature approximations are equivalent to low-$\boldsymbol{\Omega}$ and low-$\boldsymbol{\rho}$ approximations, and can be derived from (4.11) by a first-order power-series expansion of the continuity equation about $[\rho_e]^i = 0$,

$$\partial_{\bar{t}}\rho_1 = -\overline{B}\left(\overline{B}\rho_1 + \partial_{\bar{r}}\rho_2\right) + \partial_{\bar{r}}^2\rho_1 \tag{4.13a}$$

$$\partial_{\bar{t}}\rho_2 = \partial_{\bar{r}}\left(\overline{B}\rho_1\right) + \partial_{\bar{r}}^2\rho_2. \tag{4.13b}$$

Under a basis transformation, the transport equations of Genack and Redfield are recovered.[1] The equivalence will be discussed in Section 4.3.

4.2 Steady state solution and a set of one-spin-species Langevin paramagnetic equations

The steady state of Equation 4.11 is developed by setting each $[j_e]_i = 0$. This yields the system of differential equations, written in components of the polarization basis,

$$\partial_{\bar{r}}\rho_1 = 0 \tag{4.14a}$$

$$\partial_{\bar{r}}\rho_2 = -\overline{B}\left(1 - \rho_2^2\right)\operatorname{arctanh}\rho_1. \tag{4.14b}$$

The solution to the system in terms of unknown thermodynamic potential constants $\Omega^i(0)$ is

$$\rho_1(\bar{r}) = -\tanh\Omega^1(0) \tag{4.15a}$$

$$\rho_2(\bar{r}) = -\tanh\left(\Omega^2(0) - \frac{\widetilde{B}(\bar{r}) - \widetilde{B}(0)}{B_d}\Omega^1(0)\right). \tag{4.15b}$$

The corresponding thermodynamic potentials in the polarization dual basis are

$$\Omega^1(\bar{r}) = \Omega^1(0) \tag{4.16a}$$

$$\Omega^2(\bar{r}) = \Omega^2(0) - \frac{\widetilde{B}(\bar{r}) - \widetilde{B}(0)}{B_d}\Omega^1(0). \tag{4.16b}$$

If we assume that the *Langevin paramagnetic equation* describes equilibrium magnetization distributions of each spin-species, the unknown constants are found to be

$$\Omega^1(0) = \frac{\mu_2 B_d}{k_B T} \tag{4.17a}$$

$$\Omega^2(0) = -\frac{\mu_2\overline{B}(0)}{k_B T} \tag{4.17b}$$

where T is the temperature of the sample. In this case, we can rewrite the steady state solutions

---

[1] See Genack and Redfield (1975), p. 83. We have assumed a single transport rate.

as

$$\rho_1(\bar{r}) = -\tanh\frac{\mu_2 B_d}{k_B T} \tag{4.18a}$$

$$\rho_2(\bar{r}) = \tanh\frac{\mu_2 \widetilde{B}(\bar{r})}{k_B T} \tag{4.18b}$$

and

$$\Omega^1(\bar{r}) = \frac{\mu_2 B_d}{k_B T} \tag{4.19a}$$

$$\Omega^2(\bar{r}) = -\frac{\mu_2 \widetilde{B}(\bar{r})}{k_B T}. \tag{4.19b}$$

This result is a set of Langevin paramagnetic equations. If the system is in thermal equilibrium, (4.18) and (4.19) yield its expected steady state. In the general steady state case, (4.15) and (4.16) are valid, yet have coefficients $\Omega^i(0)$ that may be unknown. Those constants are determined in (4.18) and (4.19) with the physical assumptions of Langevin and Curie.

4.3 Equivalence to other models at high spin-temperatures

In Section 4.1.6 (High spin-temperature magnetization transport equation), we asserted that the linear transport equation developed there is equivalent to the transport equations of Genack and Redfield.[2] Here we show the basis transformation that yields this equivalency. Additionally, another commonly encountered form of the linear model—one expressed in inverse spin-temperature variables—is shown to be equivalent.

Two methods are used to verify the equivalency of the equations. The first is to relate Genack and Redfield's basis to the polarization basis, derive the nonlinear equation in terms of their components via Proposition 3.1, and linearize it for small $\boldsymbol{\rho}$-quantities. The component transformation from the (inhomogeneous) Genack and Redfield basis to the (inhomogeneous) polarization basis is given by the $(1,1)$-tensor transformation $R : \mathcal{O}^* \to \mathcal{O}^*$, which has the matrix representation

$$R = \frac{1}{\mu_2 \Delta_2}\begin{bmatrix} -B_d/\mu_0 & 0 \\ 0 & 1 \end{bmatrix} \tag{4.20}$$

where μ_0 is the magnetic constant.[3]

The second method is to directly transform the Genack and Redfield equations into (4.13) via (4.20). Let $[\rho_{gr}]_1$ and $[\rho_{gr}]_2$ denote the magnetic susceptibility and magnetization, respectively.[4]

---

[2] Equations (24a,b) of Genack and Redfield (1975) are the equivalent expression. We believe that (24b) has a typo in the term containing the current (it is missing a negative sign), but it is otherwise equivalent.

[3] See NIST (2010), p. 1. The appearance of the magnetic constant is due to Genack and Redfield's definition of dipole energy-density as the magnetization times $-B/\mu_0$ (Genack and Redfield, 1975, p. 83).

[4] We use the definitions of Genack and Redfield.

Both the variables and the equations must be transformed by the relations

$$[\rho_e]_i = [R]_i{}^j [\rho_{gr}]_j \text{ and} \tag{4.21a}$$

$$\partial_t [\rho_e]_i = [R]_i{}^j \partial_t [\rho_{gr}]_j . \tag{4.21b}$$

Both methods have been used to verify the equivalency. The latter method is valid only because both bases shared the same zero-state, about which each system was linearized.

Eberhardt *et al*. and others express this high spin-temperature model in terms of inverse spin-temperatures (Genack and Redfield, 1975; Eberhardt et al., 2007; Ramanathan, 2008). It is tedious but straightforward to show that these are equivalent to linearized equations in $\boldsymbol{\rho}$ that have been transformed to equations in $\boldsymbol{\Omega}$ via a linearized version of (4.7), under the following choice of basis: $[\rho_{st}]_1$ is the dipole-energy density in $\mathrm{J\,m^{-3}}$ and $[\rho_{st}]_2$ is the Zeeman energy density in $\mathrm{J\,m^{-3}}$. The component transformation from the standard basis to this (inhomogeneous) basis is given by the $(1,1)$-tensor transformation $M : \mathcal{O}^* \to \mathcal{O}^*$, which has the matrix representation

$$M = \begin{bmatrix} 1 & B(r) \\ 0 & -B(r) \end{bmatrix} . \tag{4.22}$$

The linearized map of the components of this basis to the components of its thermodynamic dual basis is given by the $(2,0)$-tensor transformation $N : \mathcal{O}^* \to \mathcal{O}$, which has the matrix representation

$$N = \frac{-1}{\mu^2 \Delta^2} \begin{bmatrix} 1/B_d^2 & 0 \\ 0 & 1/B(r)^2 \end{bmatrix} . \tag{4.23}$$

The $\boldsymbol{\rho}$-variable equation is transformed to the $\boldsymbol{\Omega}$-variable equation by the relations

$$[\Omega_{st}]^i = [N]^{ij} [\rho_{st}]_j \text{ and} \tag{4.24a}$$

$$\partial_t [\Omega_{st}]^i = [N]^{ij} \partial_t [\rho_{st}]_j . \tag{4.24b}$$

In summary, the $\boldsymbol{\rho}$-variable and $\boldsymbol{\Omega}$-variable expressions of Genack and Redfield's model are both equivalent to the high spin-temperature limit of the model of magnetization transport here presented. We consider this to be a form of *validation* of the models of Chapter 3 and Chapter 4, and especially the entropy density function of Definition 3.4.

4.4 The Fenske equation

Fenske developed a set of equations to describe the process of mass separation in the fractional distillation of hydrocarbons (Fenske, 1932). These have become the standard for simple models of mass separation.[5] In this section, a model will be derived in the manner of Fenske that is equivalent to a linearized form of the steady state model of one-species magnetization transport presented above. This will highlight the separative aspect of magnetization transport, even in the one-species case.

Consider the discrete system illustrated in Figure 4.1. It is analogous to a fractional distillation column in which "tray" i contains a certain ratio of one substance to another, and tray $i+1$ contains a greater concentration. Figure 4.1 shows two "spin" trays in which the two "substances" are spin-up and spin-down, described by the fractions $\xi_i^\uparrow$ and $\xi_i^\downarrow$. Let the total amount of spin in a tray be fixed:

$$\xi_i^\uparrow + \xi_i^\downarrow = 1. \tag{4.25}$$

Through an exchange process among the trays, tray $i+1$ obtains a higher ratio between up- and down-spin. In a fractional distillation column, concentration occurs by boiling liquid in a tray, the vapor of which condenses in the tray above and contains a higher concentration of the product, and fluid flows downward for mass balance. In the spin system, the exchange occurs through dipole-dipole interactions. Let $\alpha \geqslant 1$ be the *relative volatility* (typically α is not much larger than unity). The Fenske model describes this process by the relation[6]

$$\frac{\xi_{i+1}^\uparrow}{\xi_{i+1}^\downarrow} = \alpha \frac{\xi_i^\uparrow}{\xi_i^\downarrow}. \tag{4.26}$$

Let $\xi_0^\uparrow$ and $\xi_0^\uparrow$ be the spin fractions of some reference tray (0). Equation 4.26 is a difference equation that can be solved in the steady-state for the *Fenske equation*[7,8]

$$\frac{\xi_i^\uparrow}{\xi_i^\downarrow} = \alpha^i \frac{\xi_0^\uparrow}{\xi_0^\downarrow}. \tag{4.27}$$

A continuum solution is found if tray i is taken to be spatially small and mapped to the dimensionless spatial coordinate $\bar{r}$ (i.e. $i \to \bar{r}$). Polarization can be identified as

$$[\rho_e]_2(\bar{r}) = 2\xi_{\bar{r}}^\uparrow - 1 = 1 - 2\xi_{\bar{r}}^\downarrow \tag{4.28}$$

Equation 4.27 can be written in terms of polarization. What is more interesting, however, is that for α near unity, the following equation is approximate (and exact in the limit):

$$[\rho_e]_2(\bar{r}) = \tanh\left(a\bar{r} - b\right) \tag{4.29a}$$

---

[5] See Kister (1992), p. 114.

[6] See Halvorsen and Skogestad (2000), p. 35.

[7] This is not the usual form of the Fenske equation, but it is equivalent.

[8] The superscript of α is not an index, but an exponent.

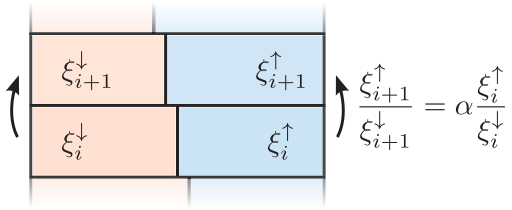

Figure 4.1: Two "trays" containing fractions of up-spin $\xi^{\uparrow}$ and down-spin $\xi^{\downarrow}$. The fraction ratio in tray $i+1$ is related to that of tray i by the relative volatility α.

where

$$a = \frac{\alpha - 1}{\alpha + 1} \qquad \text{and} \qquad b = -\operatorname{arctanh}[\rho_e^0]_2. \tag{4.29b}$$

Considering Equation 4.15 (Steady state solution and a set of one-spin-species Langevin paramagnetic equations), the following identification can be made in the linear limit:

$$\alpha = \frac{1 + \partial_{\bar{r}} \rho_2}{1 - \partial_{\bar{r}} \rho_2}. \tag{4.30}$$

Recalling the definition of the static SMT figure of merit κ of Equation 3.23 (static SMT figure of merit) and identifying $\bar{c} \to \overline{B}$, we write

$$\alpha = \frac{1 + \kappa}{1 - \kappa}. \tag{4.31}$$

This result connects the theory of separative magnetization transport with Fenske-style separation theory. For separation to occur, the relative volatility α must be non-unity and the SMT parameter κ must be nonzero. These are two statements of the same rule.

This highlights the separative nature of transport in the spin system. Small concentrations of magnetization develop in the steady-state, and this can be considered separation of up-spin and down-spin. Significantly increasing $|\kappa|$ by the methods of Section 3.6 (Static and dynamic SMT figures of merit) is difficult to imagine for a single species, unlike with a second spin-species as presented in Chapter 3. This was, in fact, the motivation for the two-species model. SMT occurs without the second species, but it is difficult to enhance due to too few parameters that can be manipulated experimentally. The two-species model has more parameters to explore in order to increase SMT. In particular, the magnetization of one species, which can be easily manipulated experimentally, can be used to increase SMT.

Chapter 5

Numerical investigations of the two spin-species model

The SMT figures of merit developed in Section 3.6 (Static and dynamic SMT figures of merit) can guide the search of the system parameters for greater separation. The development of the model of Chapter 3 (Modeling magnetization transport: two spin-species) was preceded by a rudimentary two spin-species analysis from which an experiment was designed and performed, as described in Appendix A (Measuring separative magnetization transport). In this chapter, we numerically investigate the experimental results. Additionally, we investigate a potential experiment that could be performed to validate the model of Chapter 3.

5.1 Numerical investigation of performed experiment

The experiment was based on an early analysis of SMT that indicated that, in a two spin-species system, significant separation in one species would occur if a gradient was induced in the distribution of the other. This gradient is readily achieved by applying a magnetic-resonant field oscillating at the Larmor frequency of that spin-species, which can either invert or "saturate" (randomize the direction of the spins) its magnetization, locally, leaving a region of transition with a potentially large gradient.

Significant local nuclear hyperpolarization was expected in the experiment when the electron magnetization was saturated by an oscillating field. These gains were to measured by inverting the nuclear magnetization in the hyperpolarized region and measuring the phase-shift of the oscillator's response (see Appendix A). However, these expectations were not observed in the data. One of the primary motivations of the development of the detailed model of Chapter 3 was to understand this lack of hyperpolarization. In this section, these results are explained with the model.

Symbol	Definition	Value
$B(0)$	background magnetic field	89.3 mT
$\partial_r B\|_{r=0}$	background magnetic field gradient	$44 \times 10^3\ \mathrm{T\,m^{-1}}$
T	temperature of the sample	10 K
Δ_2	nuclear spin density (polystyrene, 96%)	$1.513 \times 10^{29}\ \mathrm{m^{-3}}$
Δ_3	electron spin density (DPPH, 4%)	$8.552 \times 10^{25}\ \mathrm{m^{-3}}$
B_d	maximum dipole-dipole magnetic field	0.59 mT

Table 5.1: Parameters used to simulate the performed experiment.

The parameters used to simulate the experiment are tabulated in Table 5.1. These approximate the conditions of the experiment described in Appendix A (Measuring separative magnetization transport).

We simulate the system with Equation 3.15 (two-species magnetization transport equations). The effect of the oscillating field is introduced by adding the following term to the $[\rho_e]_3$-equation: $([\rho_e^0]_3 - [\rho_e]_3)/\tau$, where $[\rho_e^0]_3$ describes the profile of $[\rho_e]_3$ under the effects of the oscillating magnetic field and τ is some small (dimensionless) time (the smaller it is, the faster the $[\rho_e]_3$ approaches $[\rho_e^0]_3$).

The boundary conditions are chosen to be $[j_e]_i = 0$, in accordance with Equation 3.17 (Steady state solution and the two-species SMT parameters). This is true to the experimental conditions at the left-hand boundary, consider this boundary in the experiment was the surface of the sample, and therefore no flow can escape. The right-hand boundary is somewhat artificial (the sample is thick enough to be considered semi-infinite). However, if, in simulation, it is chosen to be far-enough away from the dynamics, it has no significant effect. The boundaries are chosen to be at $r = \pm 100$ nm or $\bar{r} \approx \pm 7.512$.

The initial conditions were chosen to be the thermal equilibrium distributions of Equation 3.21 (Multi-spin-species Langevin paramagnetic equations), with the exception of a region of near-zero electron magnetization imposed by the oscillating magnetic field. This ρ_3-distribution was maintained throughout the simulation by including the τ-term described above.

The equations were simulated for $t \in [0, 1]$ s or $\bar{t} \in [0, 22.7]$ with a region of near-zero electron magnetization at the surface of the sample, which is consistent with the experimental protocol. Figure 5.1 shows the main results of the simulation: the spacetime-evolution of $\boldsymbol{\rho}$ and $\mathbf{j}$. The explanation for the lack of detected signal in the experiment is readily apparent from the plot of ρ_2: *very little separation occurred*. From the rudimentary analysis that guided the experimental design, the nuclear polarization ρ_2 was expected to accumulate a negative polarizations near the surface of magnitude greater than the initial polarization. However, no significant amplification of the signal is predicted, which is consistent with the experimental result.

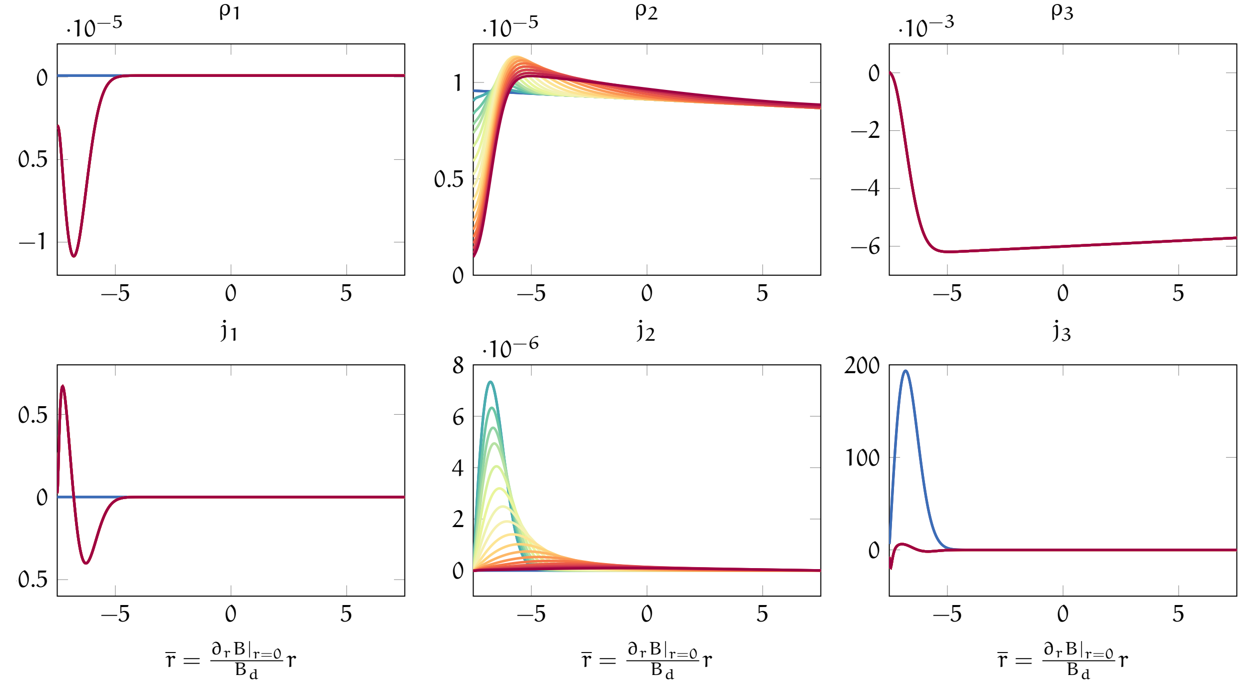

Figure 5.1: Simulation of the performed experiment. The spacetime-evolution of the spatial distributions of $\boldsymbol{\rho}$ and $\mathbf{j}$ in the polarization basis is shown. Time varies logarithmically (more values early on), with the color of the traces varying with t in seconds: 0 ▬ 1. The dipole energy density ρ_1 quickly reacts to the electron polarization ρ_3 gradient. The nuclear polarization ρ_3 responds relatively slowly. In the experiment, the nuclear polarization was inverted and measured at time $t = 1$ s.

We see that the nuclear current of Definition 3.8 (two-species current),

$$j_2 = -\bar{c}\left(1 - \rho_2^2\right) \operatorname{arctanh} \rho_1 - \partial_{\bar{r}} \rho_2,$$

starts high and dissipates. This is because the developing gradient of nuclear polarization $\partial_{\bar{r}}$ cancels the dipole energy density ρ_1 term that had been driving the nuclear polarization current. This is equivalent, in the equation for ρ_2, to the diffusive term matching the separative term. Recall that the separative term is concentrating the distribution of ρ_2 (“hyperpolarizing”), while the diffusive term is “smoothing” it.

Figure 5.2 shows the temporal evolution of the dynamic figure of merit λ and its cumulative temporal integral. The separative transport quickly stalls, allowing the diffusive term to cancel it. The reason that λ is very similar to j_1 is that j_1 is proportional to $\partial_{\bar{r}}\rho_1$, which also appears in λ. This means $\partial_{\bar{r}}\rho_1$ is the dominant term in λ. That is, in this case, the dynamic separative transport is dominated by the gradient of the dipole energy density.

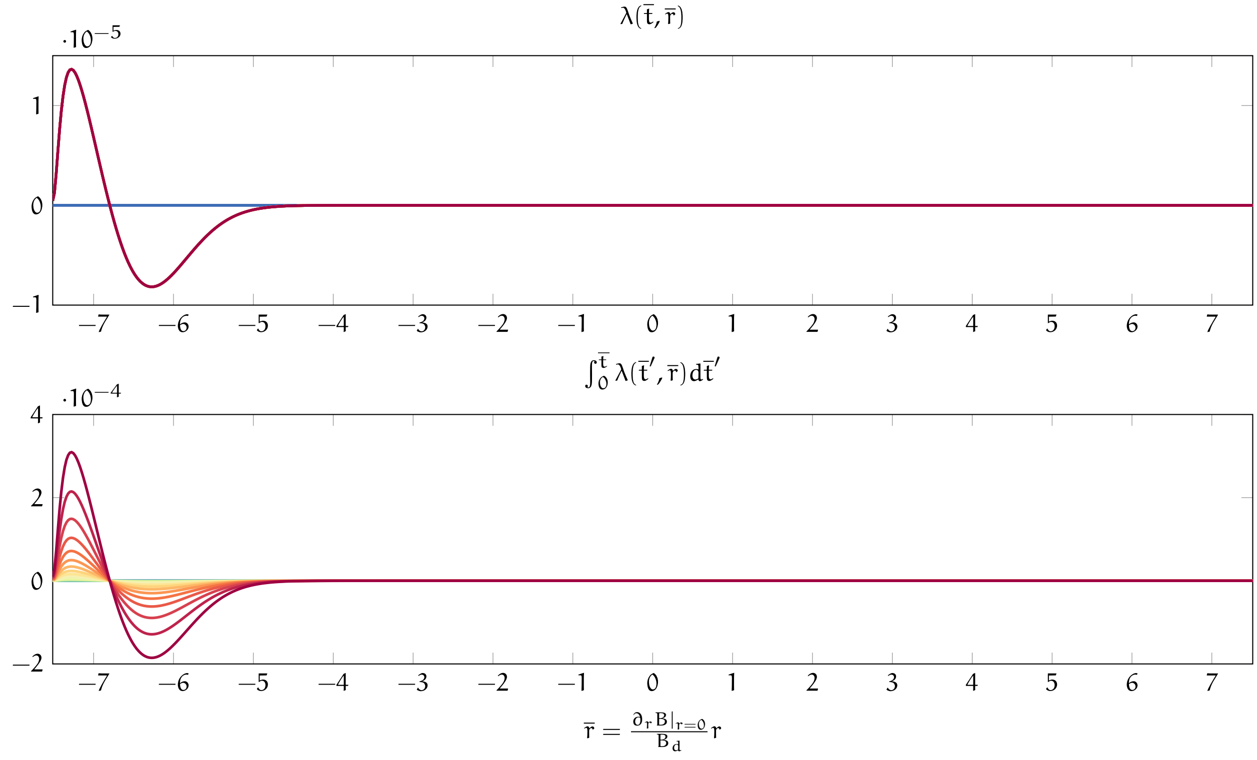

Figure 5.2: Simulation of the performed experiment. The time-evolution of the spatial distributions of the dynamic figure of merit λ and its cumulative temporal integral are shown. Time varies logarithmically (more values early on), with the color of the traces varying with t in seconds: 0 ▬ 1.

5.2 Numerical investigation of potential experiments

In this section, we numerically investigate an experiment that could be performed to validate the two-species model. In it, the polarization in a slice of the sample is doubled in approximately 3 ms. If a signal can be measured from an inversion of the slice before this doubling, twice that signal will be measured afterwards.

The parameters used to simulate the experiment are tabulated in Table 5.2. These values are typical for a magnetic resonance force microscopy (MRFM) experiment. Notice that the magnetic field and its gradient are greater than those used in the last section. The greater field yields a greater thermal equilibrium polarization, making it easier to measure a signal before any SMT is induced. The greater gradient generates hyperpolarization faster. Both are advantageous in practice.

As before, we simulate the system with Equation 3.15 (two-species magnetization transport equations) and introduce the effect of the oscillating field by adding the term $([\rho_e^0]_3 - [\rho_e]_3)/\tau$ to the $[\rho_e]_3$-equation. Similarly, the boundary conditions are $[j_e]_i = 0$ and the boundaries are at

Symbol	Definition	Value
$B(0)$	background magnetic field	2.7 T
$\partial_r B\vert_{r=0}$	background magnetic field gradient	4.4×10^{6} T m^{-1}
T	temperature of the sample	10 K
Δ_2	nuclear spin density (polystyrene, 99%)	1.561×10^{29} m^{-3}
Δ_3	electron spin density (DPPH, 1%)	2.138×10^{25} m^{-3}
B_d	maximum dipole-dipole magnetic field	0.48 mT

Table 5.2: Parameters used to simulate the proposed experiment.

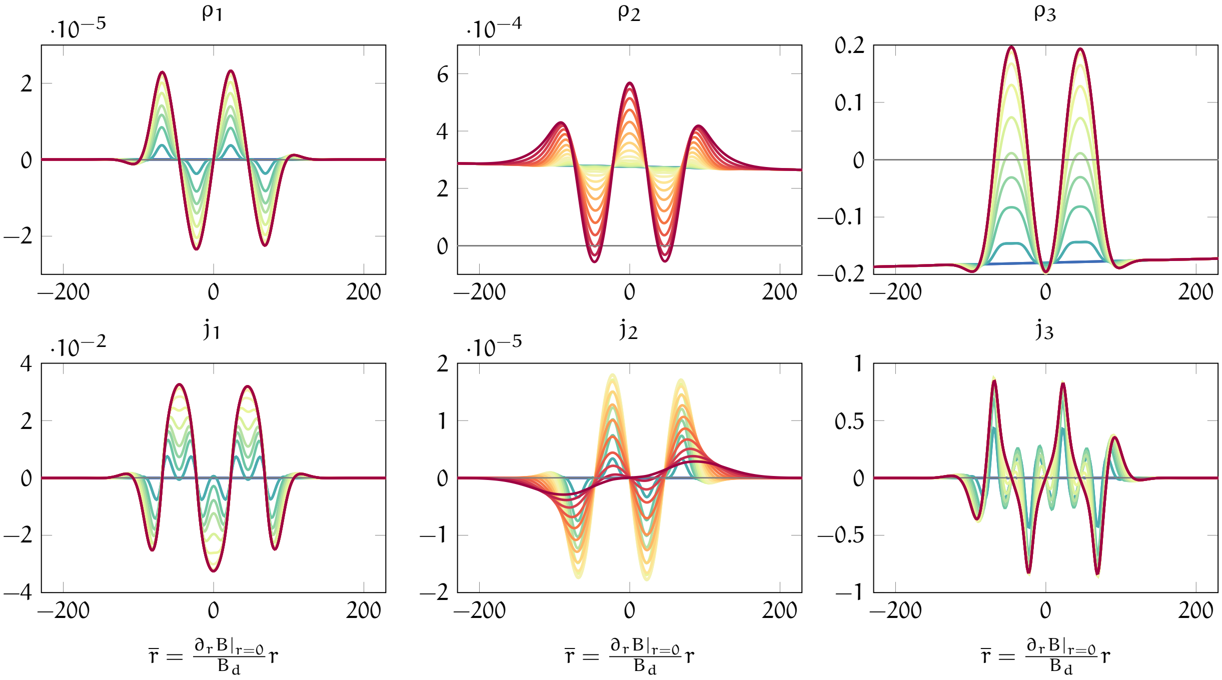

Figure 5.3: Simulation of the proposed experiment. The time-evolution of the spatial distributions of $\boldsymbol{\rho}$ and $\mathbf{j}$ in the polarization basis is shown. Time varies logarithmically (more values early on), with the color of the traces varying with t in seconds: 0  0.003. The two electron polarization (ρ_3) inverted slices create a variation in dipole energy density (ρ_1), which drives the nuclear SMT. We see a local doubling of nuclear polarization near the origin.

$r = \pm 50$ nm or $\bar{r} \approx \pm 458$.

The initial conditions were chosen to be the thermal equilibrium distributions of Equation 3.21 (Multi-spin-species Langevin paramagnetic equations), with the exception of two regions of inverted electron magnetization imposed by the oscillating magnetic field. This ρ_3-distribution was maintained throughout the simulation by including the τ-term described above.

Two adjacent regions of the electron polarization are inverted away from the boundaries of the sample, which is unlike the single region of near-zero polarization induced at the surface in

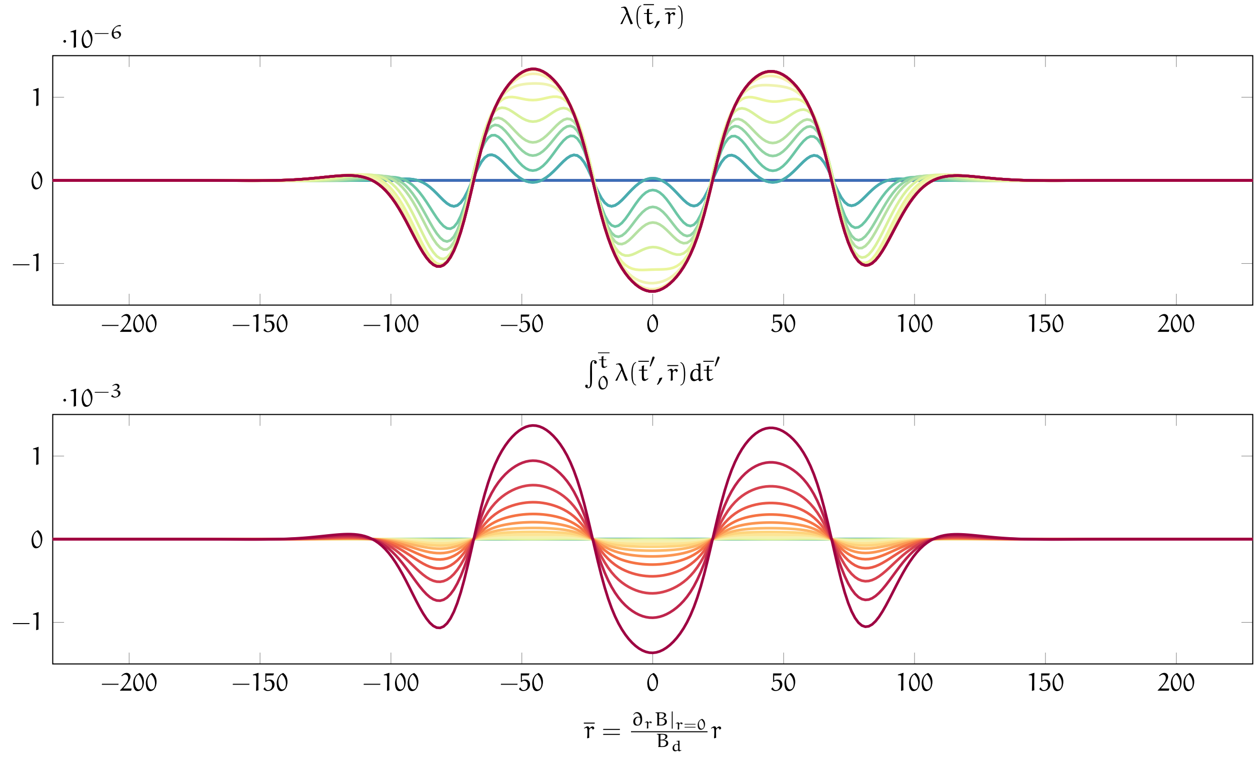

Figure 5.4: Simulation of the proposed experiment. The spacetime-evolution of the spatial distributions of the dynamic figure of merit λ and its cumulative temporal integral are shown. Time varies logarithmically (more values early on), with the color of the traces varying with t in seconds: 0 ▬ 0.003.

Section 5.1. Figure 5.3 shows the predicted spacetime-evolution of the distribution of $\boldsymbol{\rho}$ and $\mathbf{j}$. Near $\bar{r} = 0$, in a slice of width approximately 5 nm, a doubling of the nuclear polarization occurs in 3 ms. This corresponds to a doubling in signal for the protocol described in Appendix A (Measuring separative magnetization transport).

However, we see that the nuclear current quickly diminishes, as before. Once again, the dipole energy stagnates and diffusion, increasing due to the increased curvature, becomes strong enough to counterbalance its separative effects.

The dynamic SMT figure of merit λ and its cumulative integral, shown in Figure 5.4, tell a similar story to that of the last section. The gradient of ρ_1 dominates the dynamic separation, which eventually stagnates. This stagnation allows the diffusive term to counter the separative term and drive the system toward an equilibrium.

Chapter 6

Conclusions & prospects

A study of separative magnetization transport for one- and two-species spin systems has been presented. This thesis is not the last word on the subject, but the first. The groundwork for further study is now laid upon a well-posed foundation of the following elements.

framework for transport analysis In Chapter 2 we developed a theoretical framework for transport analysis (Proposition 2.2) that can be applied to model the transport of systems with any number of globally conserved quantities in any spatial configuration by supplying the following (as described in Remark 2.2):

(a) a spatial manifold, metric, and local coordinates;
(b) globally conserved thermodynamic quantities that define local quantity densities;
(c) a local entropy density function; and
(d) a transport rate tensor.

This framework guarantees that models derived from it will respect the four laws of thermodynamics (Proposition 2.1).

two-species model In Chapter 3 we derived an analytically tractable model (Proposition 3.1) of systems with two spin-species and (therefore) three conserved quantities. This model exhibits both diffusive and separative qualities, and so it can be used to explore the possibility of harnessing separative magnetization transport for hyperpolarizing nuclear magnetization. As a model that is valid for high-polarization regimes, it can be used for systems that have been hyperpolarized by other means, such as dynamic nuclear polarization. In Chapter 4 a one-species model is derived as a special case of the two-species model. It is also valid for high-polarization regimes. In the limit of low-polarization, it is shown to be consistent with the model of Genack and Redfield, which is understood as a validation of the models from which the low-polarization model was derived.

entropy density function As described in Remark 2.2, an entropy function is required to model the system with the framework of Chapter 2. In Section 3.1, we presented such an entropy density function to describe the two-species system. It was used to derive the two-species model of Proposition 3.1. Although the dynamical behaviour of the model is not particularly sensitive to the functional form of the entropy (of course, it must satisfy the requirements of the framework), the analytic tractability of the model is. The entropy function of Definition 3.4 yields a model that is simple enough to gain insight from analysis.

An alternative entropy function is presented in Appendix B. When the dipole energy of a system is small compared to unity, which is most often the case, the two entropy density functions yield nearly identical dynamics. When the dipole energy is large, the physical justification of the function presented in Appendix B may be superior. Both entropy density functions can be shown to predict the classic result of Genack and Redfield, as demonstrated in Chapter 4 and Picone et al. (forthcoming).

figures of merit In Section 3.6, we identified a static and a dynamic figure of merit. These figures of merit allow the parameter-space of a two-species system to be explored in search of greater SMT. The static figure of merit is derived from the steady state solution of the two-species model. It is a metric for the slope of the steady state distribution of nuclear polarization. The dynamic figure of merit is derived from the dynamic two-species model. It is a metric for the separative (non-diffusive) term in the nuclear polarization equation.

numerical investigations In Chapter 5, the two-species model was used to simulate the experiment described in Appendix A. The results explain the null result of the experiment. A new experiment was proposed and simulated that was predicted to have a measurable hyperpolarization from SMT. Such an experiment would be a validation of the two-species model and a step toward greater hyperpolarization through SMT, with the goal of applying it to significantly enhance magnetic resonance technologies.

Much of the preceding has been science, and much of what lies ahead for separative magnetization transport is engineering. Giddings' words frame the task so well, they are repeated (from Section 2.1):

> Separation is the art and science of maximizing separative transport relative to dispersive transport.[1]

Now that we better understand magnetization separation, we can begin harnessing it for hyperpolarization. A number of possibilities present themselves. Separative transport is eventually overtaken by diffusive transport, as described in Chapter 5. The following methods may mitigate this occurrence.

applying pulse sequences Magnetic resonance technologies have often required pulsing the oscillating magnetic field. This may allow a release of the separation/diffusion gridlock.

---

[1] See Giddings (1991), p. 10.

increasing magnetic field curvature The dimensionless ratio $\bar{c}$ is a multiplying factor of the separative transport. If the background magnetic field B has no curvature (a linear field), the $\bar{c}$ is at most unity. However, with significant curvature, an amplification of the separative transport would occur.

varying spin density The analysis above assumed uniform spin densities for each species. If these densities were varied, selective magnetization barriers may form. The analysis above is readily adopted to the sort of analysis required to explore this method.

6.1 Prospects for technology development

The theoretical framework of Chapter 2 and the two-species model of Chapter 3 have laid the groundwork for further study of separation magnetization transport. The engineering applications of this work include many magnetic resonance technologies, including magnetic resonance force microscopy (MRFM), nuclear magnetic resonance (NMR) spectroscopy, and magnetic resonance imaging (MRI). With all these technologies, greater signal-to-noise ratios (SNR) yield faster images with higher resolution. Hyperpolarization through SMT may yield appreciable increases in polarization, which is directly proportional to increases in SNR.

An alternative technology, dynamic nuclear polarization (DNP), has shown experimental progress. Its effects are diminished, however, in technologies, such as MRFM, in which large field gradients are present. DNP uses an entirely different mechanism to create hyperpolarization, which is apparent by the fact that polarization is *not* conserved, whereas in SMT, conservation is assumed. So hyperpolarization via SMT and DNP are *complementary* technologies, and it may be the case that for certain magnetic resonance technologies SMT, DNP, or some combination of both will yield the most significant progress.

6.2 Experimental roadmap

We conclude this study with an experimental roadmap for separative magnetization transport as a method of hyperpolarization. Although the model presented here is in agreement with the experimental results, it remains to be fully experimentally validated. The following objectives serve as a roadmap for future experimental investigation of SMT.

objective I: validate SMT model A validation of the SMT model may be in the context of any spatial scale. The elements involved in such an experiment would include: (i) the manipulation of one spin-species and (ii) the measurement of a resulting concentration of magnetization — of either spin species — that can be shown to be the result of (i). The "concentration" should be demonstrably greater than would be expected from non-SMT mechanisms such as background magnetic field and dynamic nuclear polarization.

objective II: explore SMT An exploration of the SMT model would include its validation, but would go further. While some features of the model will be present in a validation experiment, many may not be obvious. For instance, exploration might include a measurement of the transport coefficients, size of the affected region, and duration during which the effect increases and diminishes.

objective III: enhancement of SMT An enhancement of SMT would include both the model's validation and *directed* exploration. This objective has in mind not merely descriptive scientific inquiry, but also its teleological function in engineering. An experiment with this objective would seek to describe, for instance, the domains in which certain parameters can increase the SMT effect. This objective is dependent on the first two, but also the fourth in that those for whom this is an objective must have in mind, finally, harnessing SMT.

objective IV: harnessing SMT Harnessing SMT would require the validation and exploration SMT, and would likely build on experiments that showed methods of enhancing SMT. These experiments are at the boundary between technology development and application. Among the numerous possible uses of SMT, enhancing magnetic resonance force microscopy (MRFM) is an exemplar. MRFM is already equipped with much of the apparatus required for such an experiment and its localized detection and high sensitivity make it an attractive choice.

Bibliography

A Abragam and M Goldman. Principles of dynamic nuclear polarisation. *Reports on Progress in Physics*, 41(3):395, 1978. URL `http://stacks.iop.org/0034-4885/41/i=3/a=002`.

K. J. Bruland, J. L. Garbini, W. M. Dougherty, and J. A. Sidles. Optimal control of force microscope cantilevers. ii. magnetic coupling implementation. *Journal of Applied Physics*, 80(4):1959–1964, 1996. doi: 10.1063/1.363086. URL `http://link.aip.org/link/?JAP/80/1959/1`.

R. Budakian, H. J. Mamin, and D. Rugar. Suppression of spin diffusion near a micron-size ferromagnet. *Phys. Rev. Lett.*, 92:037205, Jan 2004. doi: 10.1103/PhysRevLett.92.037205. URL `http://link.aps.org/doi/10.1103/PhysRevLett.92.037205`.

Francesco Bullo and Andrew D. Lewis. *Geometric control of mechanical systems: modeling, analysis, and design for simple mechanical control systems*. Springer, 2005.

W. M. Dougherty, K. J. Bruland, S. H. Chao, J. L. Garbini, S. E. Jensen, and J. A. Sidles. The Bloch equations in high-gradient magnetic resonance force microscopy: Theory and experiment. *Journal of Magnetic Resonance*, 143(1):106 – 119, 2000. ISSN 1090-7807. doi: DOI:10.1006/jmre.1999.1994.

Kai W. Eberhardt, Schahrazede Mouaziz, Giovanni Boero, Jürgen Brugger, and Beat H. Meier. Direct observation of nuclear spin diffusion in real space. *Phys. Rev. Lett.*, 99:227603, Nov 2007. doi: 10.1103/PhysRevLett.99.227603.

M. R. Fenske. Fractionation of straight-run pennsylvania gasoline. *Industrial & Engineering Chemistry*, 24(5):482–485, 1932. doi: 10.1021/ie50269a003. URL `http://pubs.acs.org/doi/abs/10.1021/ie50269a003`.

J. L. Garbini, K. J. Bruland, W. M. Dougherty, and J. A. Sidles. Optimal control of force microscope cantilevers. i. controller design. *Journal of Applied Physics*, 80(4):1951–1958, 1996. doi: 10.1063/1.363085. URL `http://link.aip.org/link/?JAP/80/1951/1`.

A. Z. Genack and A. G. Redfield. Theory of nuclear spin diffusion in a spatially varying magnetic field. *Phys. Rev. B*, 12:78–87, Jul 1975. doi: 10.1103/PhysRevB.12.78. URL http://link.aps.org/doi/10.1103/PhysRevB.12.78.

J. Calvin Giddings. *Unified separation science*. Wiley, New York, 1991. ISBN 0471520896 9780471520894.

David J. Griffiths. *Introduction to Electrodynamics*. Prentice Hall, third edition, 1999.

Ivar J. Halvorsen and Sigurd Skogestad. *Distillation Theory*, chapter 2. Unknown, August 2000. URL http://www.nt.ntnu.no/users/skoge/publications/1999/DistillationTheory/original/distillationtheory.pdf.

Mehran Kardar. *Statistical physics of particles*. Cambridge University Press, 2007.

Henry Z. Kister. *Distillation design*. McGraw-Hill chemical engineering series. McGraw-Hill, 1992. ISBN 9780070349094.

Jan G. Krummenacker, Vasyl P. Denysenkov, Maxim Terekhov, Laura M. Schreiber, and Thomas F. Prisner. Dnp in mri: An in-bore approach at 1.5 t. *Journal of Magnetic Resonance*, 215(0):94 – 99, 2012. ISSN 1090-7807. doi: http://dx.doi.org/10.1016/j.jmr.2011.12.015. URL http://www.sciencedirect.com/science/article/pii/S1090780711005945.

L. D. Landau and E. M. Lifshitz. *Statistical Physics*, volume 5 of *Course of Theoretical Physics*. Pergamon Press, third edition, revised and enlarged edition, 1980.

John M. Lee. *Riemannian Manifolds: an introduction to curvature*, volume 176 of *Graduate Texts in Mathematics*. Springer, first edition, 1997.

John M. Lee. *Introduction to Smooth Manifolds*, volume 218 of *Graduate Texts in Mathematics*. Springer, second edition, 2012.

The Churchill Centre. Famous quotations and stories. Online. URL http://www.winstonchurchill.org/learn/speeches/quotations/famous-quotations-and-stories.

Qing Zhe Ni, Eugenio Daviso, Thach V. Can, Evgeny Markhasin, Sudheer K. Jawla, Timothy M. Swager, Richard J. Temkin, Judith Herzfeld, and Robert G. Griffin. High frequency dynamic nuclear polarization. *Accounts of Chemical Research*, 46(9):1933–1941, 2013. doi: 10.1021/ar300348n. URL http://pubs.acs.org/doi/abs/10.1021/ar300348n.

NIST. Fundamental physical constants–extensive listing. Technical report, National Institute of Standards and Technology, 2010.

L. Onsager and S. Machlup. Fluctuations and irreversible processes. *Physical Review*, 91:1505 – 1512, 1953.

Mark E. Peeples. Vibration suppression and control of a piezoelectric scanner with application to magnetic resonance force microscopy. Master's thesis, University of Washington, 2004.

Rico A.R. Picone, Joseph L. Garbini, and John A. Sidles. Modeling spin magnetization transport in a spatially varying magnetic field. *Journal of Magnetism and Magnetic Materials*, forthcoming. URL `http://arxiv.org/abs/1310.7540`.

C. Ramanathan. Dynamic nuclear polarization and spin-diffusion in non-conducting solids. *ArXiv e-prints*, January 2008.

George Ruppeiner. Thermodynamics: A riemannian geometric model. *Phys. Rev. A*, 20:1608–1613, Oct 1979. doi: 10.1103/PhysRevA.20.1608. URL `http://link.aps.org/doi/10.1103/PhysRevA.20.1608`.

George Ruppeiner. Riemannian geometry in thermodynamic fluctuation theory. *Rev. Mod. Phys.*, 67:605–659, Jul 1995. doi: 10.1103/RevModPhys.67.605. URL `http://link.aps.org/doi/10.1103/RevModPhys.67.605`.

Charles P. Slichter. *Principles of magnetic resonance*. Springer-Verlag, 3rd enl. and updated ed., third printing edition, 1996. ISBN 3540501576 0387501576.

M. Spivak. *Calculus On Manifolds: A Modern Approach To Classical Theorems Of Advanced Calculus*. Mathematics Monograph Series. Westview Press, 1965. ISBN 9780805390216. URL `http://books.google.com/books?id=g_EXJtkz7PYC`.

R. K. P. Zia, Edward F. Redish, and Susan R. McKay. Making sense of the Legendre transform. *American Journal of Physics*, 77:614–622, 2009.

Appendix A

Measuring separative magnetization transport

In this chapter, we will describe the measurement of SMT in general and in the specific case of an experiment performed as part of this thesis. The key objective is to lay an experimental foundation for a roadmap to enhancing magnetic resonance technologies through hyperpolarization by SMT.

A.1 Experimental objectives

The objectives of the experiment are listed below.

O1. Determine if the effects of SMT can be measured in the parameter-space which the early models predicted.
O2. Measure a nuclear spin signal enhanced by SMT.
O3. Characterize the signal by exploring a parameter-space.
O4. Obtain measurements sufficient to verify the theoretical model of SMT.

The experiment was designed to meet all four objectives. The experiment yielded results that met the first objective: the effects of SMT were not observable in the parameter space predicted in the early models. The results were inconclusive for the other objectives, but the theoretical work performed since has been motivated by what was learned. Early models predicted an effect in the region of parameter space probed in the experiment. After this prediction was verified to be inaccurate, we began seeking a more thorough model. The results of Chapter 5 (Numerical investigations of the two spin-species model) verify the experimental results: no enhanced signal should have been observed.

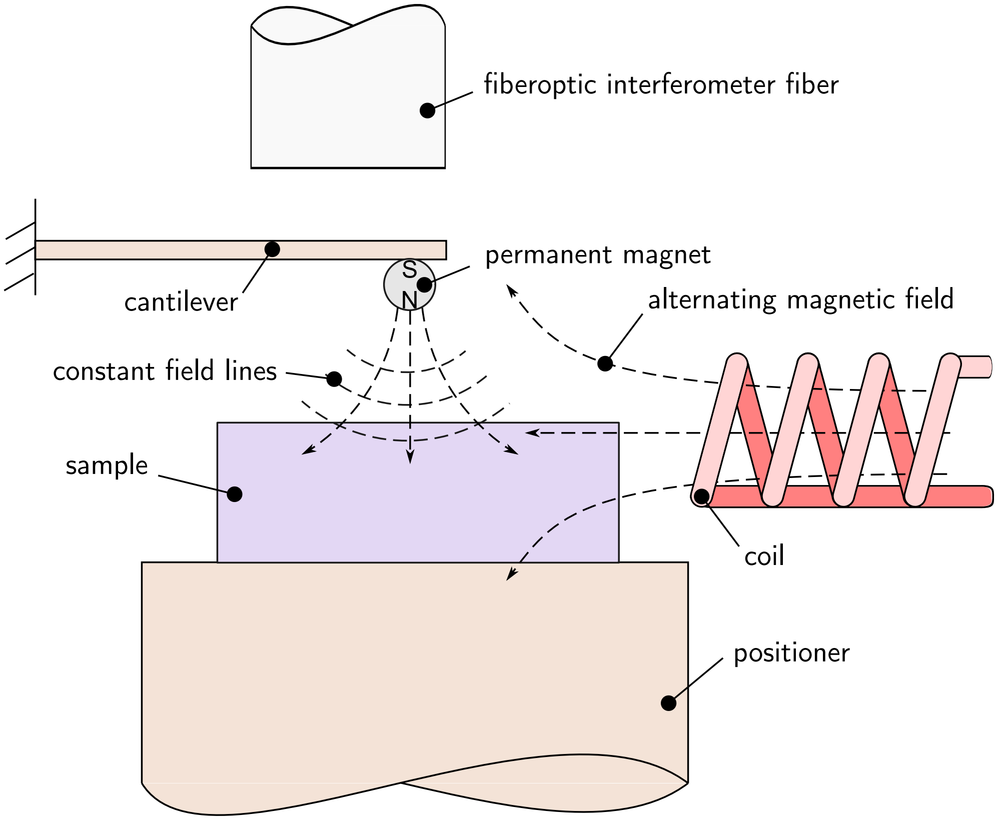

Figure A.1: A schematic of the MRFM device (not to scale).

A.2 Description of experimental apparatus

The experimental apparatus was a magnetic resonance force microscope, modified such that both radio wave and microwave magnetic fields could be applied for magnetic resonance. Each subsystem of the apparatus is described.

A.2.1 Vacuum and cryogenics

A turbomolecular pump (Oerlikon Leybold Turbotronik NT-10) evacuated a flow cryostat (Janis Research Systems, modified model ST400) to approximately 10^{-5} Torr. Without vibration isolation, the cryostat was rigidly attached to a concrete support column of the building. Optical, radio wave, microwave, sample-position, magnetic tip control, and temperature-sensing signals were transmitted into and out of the cryostat through vacuum feedthroughs. A module containing the sample and cantilever was mechanically attached to the cold head of the cryostat in a manner that minimized contact area for acoustic vibration isolation. The module was attached thermally with (99.999% purity) copper braids.

The cryostat was cooled with a flow of liquid helium (LHe), which was transferred from a

Dewar via a flexible vacuum-jacket transfer line. At high flowrates, the boiling and flow of the LHe generated vibrations which dominated other noise sources in the experiment. Low flowrates and a copper-mesh heat exchanger affixed to the end of the transfer line largely mitigated this source of mechanical noise.

A.2.2 Cantilever

The mechanical resonator (detector) was a commercial force microscope cantilever (Park Scientific Instruments, Microlever C) with spring constant k of 0.014 N/m. It had an open, triangular shape with length 320 μm, arm width 22 μm, and thickness 0.6 μm. At room temperature (293 Kelvin), the resonance frequency was 7981 Hz and the quality Q was 19000. At a cryostat temperature of 13 Kelvin, the resonance frequency was 8032 Hz and the quality Q was 51000.

A.2.3 Optics

A single-mode fiberoptic interferometer measured the position of the cantilever beam. A connectorized 90:10% optical coupler (Gould) joined the four optical fiber arms. Light from the end of one arm reflected from the cantilever (~50 μm from the fiber) was interfered with light reflecting from the end of the fiber to obtain a signal. A diode laser (Sharp LTO23, pigtail connector, 780 nm) with coherence length one millimeter produced 200 μW of coupled optical power. A photodiode amplifier (New Focus Model 2001) converted the photonic signal to an electrical signal, which was further amplified and filtered (Stanford Research Systems Model SR 560) with a high-frequency roll-off of 100 kHz.

A.2.4 Sample positioner

The piezoelectric tube actuator had rails affixed to one end upon which a cart is kinematically mounted such that it had a single degree of freedom, along the rails (in the z-direction). An optical fiber was affixed to the cart, and the sample was attached to the end of the fiber. Stick-slip control enables course-grain positioning. Precision positioning in three-dimensions was used over small distances.

A.2.5 Radio wave and microwave synthesis and modulation

Two disparate frequency-bands of alternating magnetic field B_1 were necessary for the experiment. A single three-turn, hand-wound coil delivered the signal. The 120 μm-diameter coil was wound from 30 μm wire and potted in epoxy in order to minimize inter-coil mechanical motion leading to vibrations.

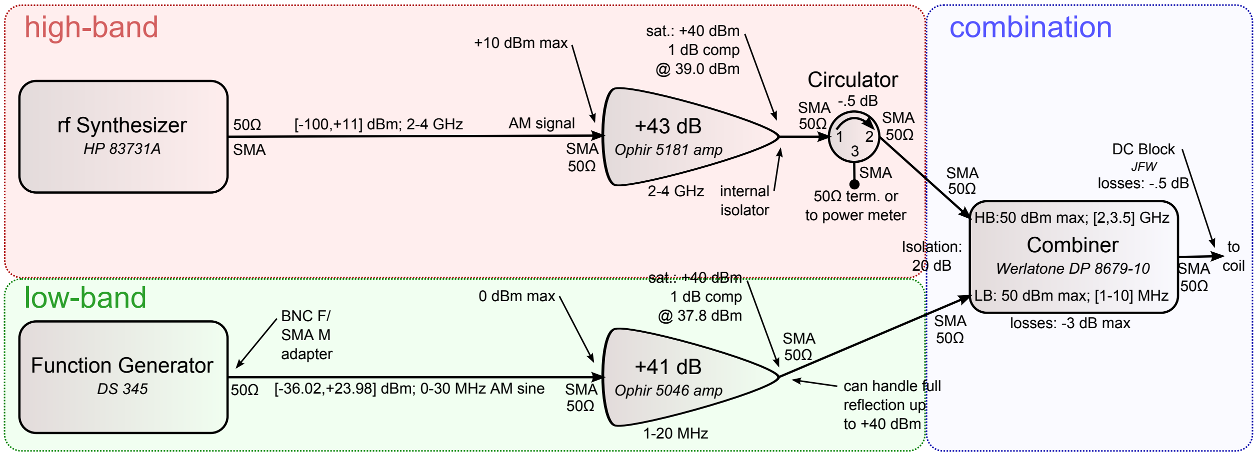

Figure A.2: A schematic of the system that generated the alternating magnetic field.

Figure A.2 is a schematic of the system that generated the alternating magnetic field. The operating range of the high-band (microwave) alternating magnetic field frequency was $[2, 3.5]$ GHz and the low-band (radio wave) range was $[3, 5]$ MHz. The high-band was generated and amplitude-modulated with a frequency synthesizer (Hewlett Packard, Model HP83731A). The low-band was generated and modulated as an arbitrary waveform with a general-purpose function generator (Stanford Research Systems, Model DS345). Each of the signals was separately amplified (Ophir RF, Models 5181 (high-band) and 5046 (low-band)). The combination of these signals was achieved with a combiner (Werlatone, Model DP 8679-10).

The input and output impedances of the system are all 50 Ohms, but the coil is "untuned," and significant reflection is anticipated and mitigated with a combination of circulator on the high-band side and amplifier specifications. The high-band amplifier has an internal output isolator and the low-band amplifier was designed to handle full reflection.

A.2.6 Sample

A solid solution of diphenylpicrylhydrazyl[1] (DPPH) in polystyrene[2] (4:96% by mass) was prepared as a dilute sample. The free-radical DPPH provided unpaired electron spins. Benzene was used as a solvent, which was allowed to evaporate from a smear of solution on a microscope slide. A small square was cut from the smear and affixed with epoxy to the end of the fiber attached to the sample-positioning cart.

---

[1] 1,1-diphenyl-2-picrylhydrazil, Sigma product number D-9132.

[2] Aldrich catalog number 18,242-7.

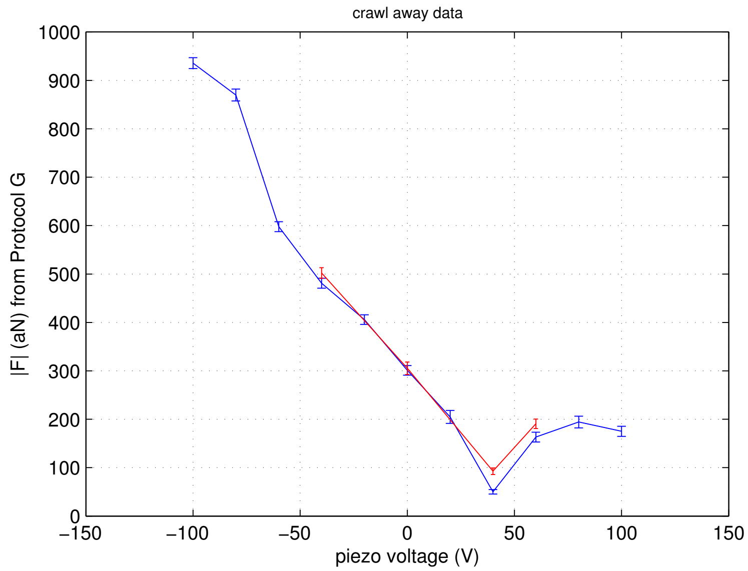

Figure A.3: Locating the sample of the surface by measuring the electron-resonant signal at various sample positions.

A.2.7 Control

There are a few feedback control systems in the microscope system: a simple cryostat temperature controller to hold the temperature steady, a gain-scheduled optimal controller of the cantilever's position (Garbini et al., 1996; Bruland et al., 1996), and a positioning controller of the sample/cart's position (Peeples, 2004).

A desktop personal computer running LabVIEW (National Instruments) controls every aspect of an experimental run through a hybrid USB/LAN/GPIB (IEEE 488) network, over which the computer sends commands to and receives data from a variety of instruments.

A.3 Experimental protocol

In this section, the experimental protocol is presented. An *initialization protocol*, at times requiring manual input, was required to cool down the system, bring the sample near the cantilever, and verify that the sample would yield an electron-resonance signal. Furthermore, a *measurement protocol*, primarily programmed into the LabVIEW software, determined the series of measurements called *runs*.

A.3.1 Initialization protocol

The following series of steps provides an outline of the initialization protocol.

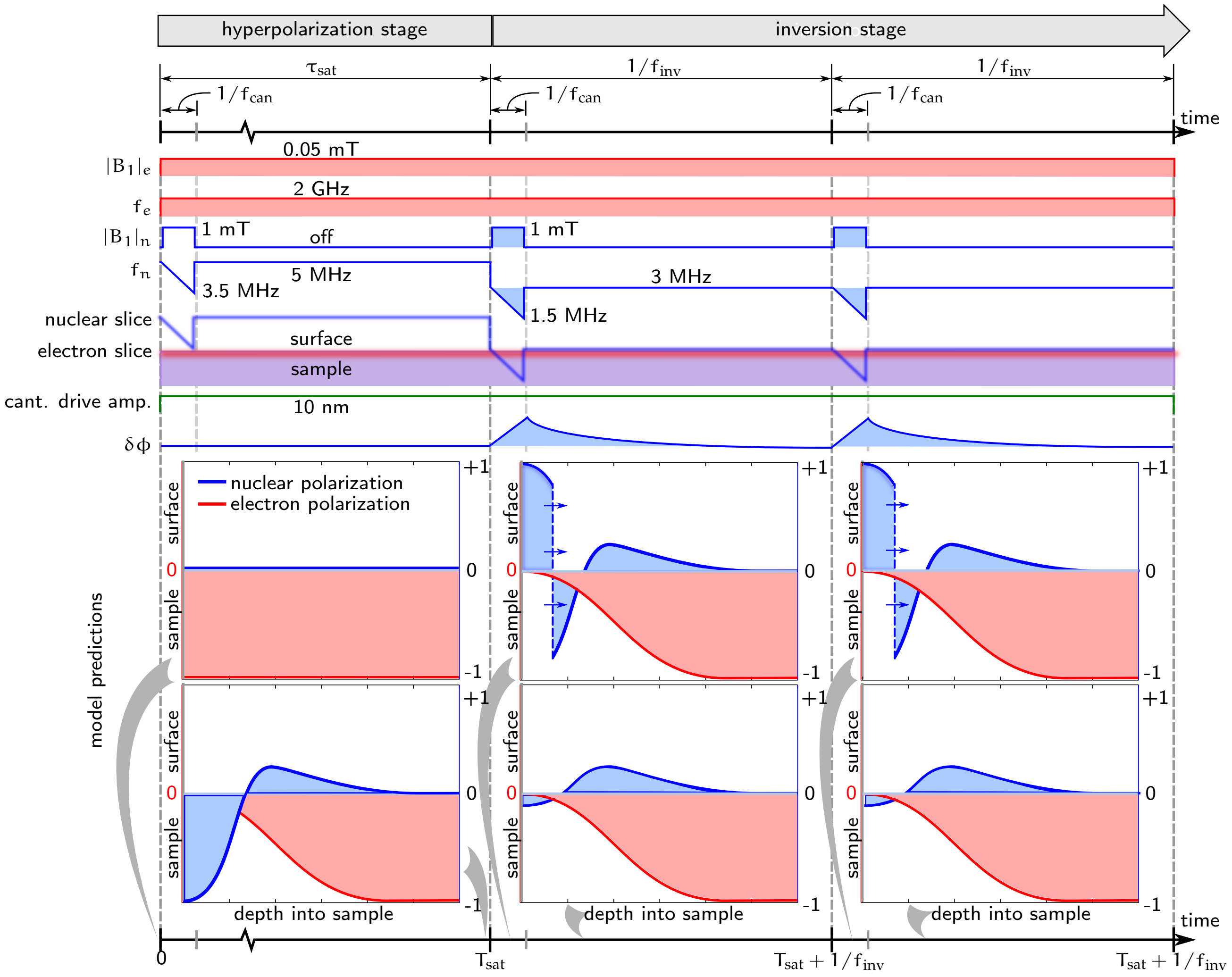

Figure A.4: A timeline of an experiment.

cooldown The experiment was cooled to 13 Kelvin over the course of a few hours. Once the transfer line of the liquid helium dewar was connected to the cryostat, the helium began to flow. After the temperature of the cryostat began to decrease, the gas-relief valve of the cryostat was opened and plumbed to the bottom of a column of water, which kept the dewar-pressure constant throughout the remaining cooldown process. When the temperature reached 13 Kelvin, the helium flowrate was decreased, a small temperature-controller was implemented (with a heating coil in the cryostat), and a period of time passed while the system came to thermal equilibrium (several hours). The dewar remained cold for approximately 48 hours after the initial cooldown.

measure parameters with sample away from cantilever The sample was stepped (via stick-slip

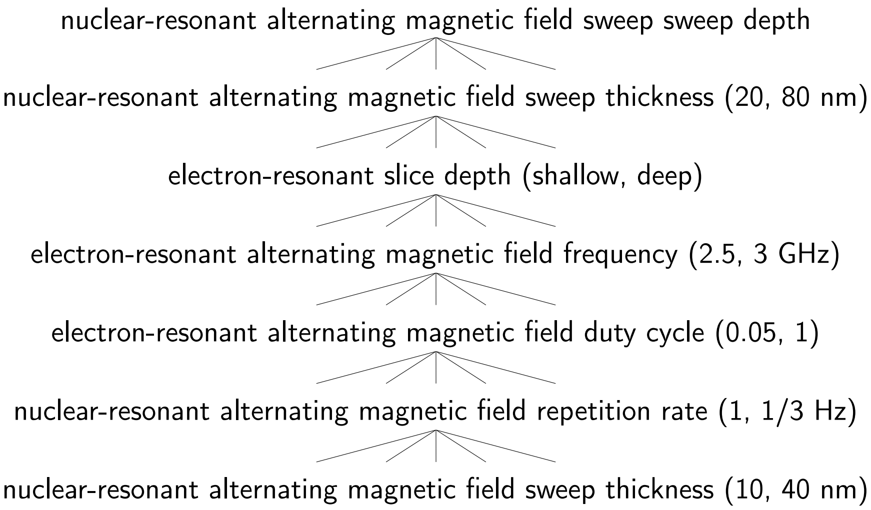

Figure A.5: Abbreviated parameter tree (first value nominal)

control) toward the cantilever until it made contact. The sample was then withdrawn to a distance sufficient to assure no sample-effects on the cantilever. In this position, a number of cantilever properties and instrument gains were measured. The noise was also evaluated, and found to be nearly thermally limited. The noise is quantified as a "noise temperature" which, using estimates of the properties of the cantilever, computes the theoretical temperature that would yield measured cantilever amplitude fluctuations through Brownian motion. Measurements yielded estimates of 13 – 20 Kelvin, indicating that the dominant noise mechanism was thermal noise, and that measurement noise was small.

approach cantilever with sample Using stick-slip control for coarse-grain positioning, approach the cantilever with the sample. The goal is to be as close as possible without contacting the cantilever and sample.

measure electron-resonance Scan the sample and attempt to measure an electron-resonant signal. Some iteration may be required.

locate the surface of the sample Once an electron-signal is established, scan and measure the signal until the surface of the sample is identified. The goal is to course-position the sample relative to the sensitive slice such that it can be linearly (fine-grain) scanned toward the cantilever — effectively moving the sensitive slice deeper into the sample — and scanned away from the cantilever — effectively moving the sensitive slice *outside* the sample (in order to make a null measurement of the coherent parasitic excitation). See Figure A.3.

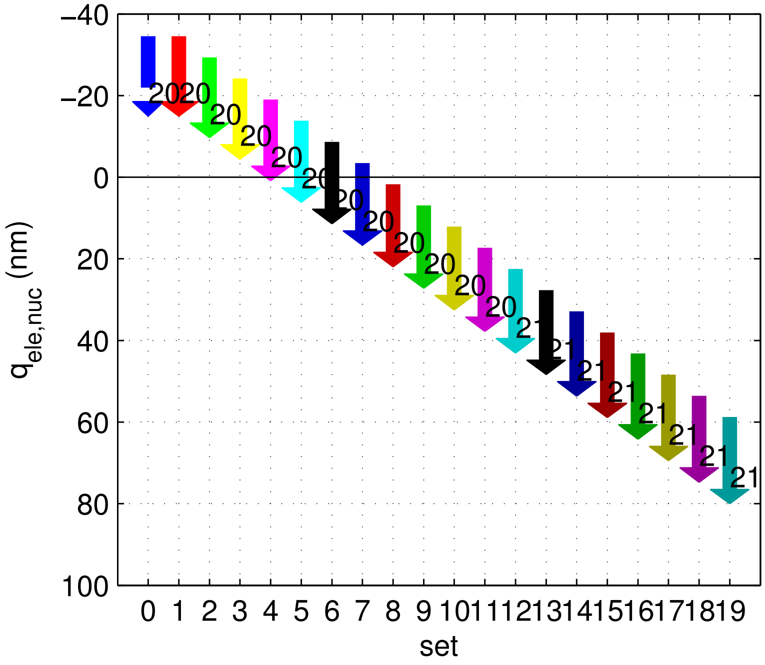

Figure A.6: An illustration of the nuclear-spin resonant frequency/spatial sweeps of Run 618. The abscissa varies the set (sets occur temporally in series) and the ordinate varies the distance from the center of the electron-resonant slice in the sample. The spatial interval through which a nuclear-resonant slice will travel during an inversion pulse within a set is depicted by a colored arrow, labeled with the number of nanometers traversed. This figure can also be used as a legend for the plots that follow.

A.3.2 Measurement protocol

The general strategy for measuring an SMT signal was to (1) induce a gradient in the electron spin polarization by saturating it with an electron-resonant alternating magnetic field in a region near the surface of the sample; (2) allow the electron-proton system to equilibrate, which the early models predicted would yield a nuclear hyperpolarization near the surface of the sample; (3) adiabatically invert the hyperpolarized nuclear-spins with a nuclear-resonant adiabatic inversion pulse; (4) drive the cantilever beam at its resonance; and (5) measure the resulting frequency shift of the response of the cantilever.

A previously prepared definition file was loaded for each run, and was executed automatically by the software. Within a run, a number of *sets* were executed, each set containing a different set of parameters (often a single parameter varied among the sets, like the sweep-depth of a nuclear-resonant alternating field sensitive slice). Within a set, a number of *repetitions* were executed for averaging, with some interval of time in between repetitions to allow the spin-cantilever system to return to equilibrium.

A timeline of a set is illustrated in Figure A.4. A description of this timeline will familiarize the reader with the primary elements of any set. The *hyperpolarization stage* includes electron-resonant rotating magnetic field irradiation, but no nuclear-resonant inversion pulses. In some runs, the electron-resonant field was pulsed. During this stage, SMT occurs such that nuclear-spins near the surface of the sample become hyperpolarized. This is a convenient time for "null" nuclear-resonant field pulses which sweep regions strictly *outside* the sample (as shown in the figure). After this stage (typically one second or some fraction thereof), an event introduces a new stage: a nuclear-resonant inversion pulse is swept through a region adjacent to the surface of the sample — presumably where the hyperpolarization will have formed — and invert the nuclear-spins. This inversion will cause a change in the spring-like moment of the nuclear spins on the cantilever, which is being driven at a constant amplitude (typically ten nanometers). This change will induce a shift in the resonance frequency of the cantilever, which yields a shift in the measured phase of the response of the cantilever.

The parameter space was explored in the following manner. We ranked the priority of the variation of each parameter and adaptively searched. The searched parameters are shown in descending order of priority in Figure A.5. Not all, but many, possible parameter-combinations were explored.

A.4 Cantilever response

To measure the spatial and temporal distribution of nuclear magnetization is our aim, which is realized indirectly by monitoring position of the cantilever as we manipulate the nuclear magnetization. Our model is incomplete without a description of the interaction of the cantilever and nuclear magnetization, so one is here presented.

From (Dougherty et al., 2000, p. 108), we can estimate the pressure (force per unit slice area) exerted by the magnetic moments of an ensemble of nuclear spins on magnetic tip of the cantilever to be

$$P = \int_{-\infty}^{\infty} \left(\partial_z B(z)\right) [\rho_\varepsilon]_2 \, dz \tag{A.1}$$

where $[\rho_\varepsilon]_2$ is the magnetic moment of nuclear spins.

A.4.1 Dynamics of the cantilever

We can write a Hamiltonian for the cantilever as

$$H(q,p) = \frac{p^2}{2m} + \frac{1}{2}kq^2 + V^*(q,t), \tag{A.2}$$

where q and p are respectively the position and momentum coordinates, k is the "native" spring constant of the cantilever when the nuclear magnetization is in equilibrium,[3] and $V^*(q,t)$ is a potential function associated with the interaction energy between the magnetic tip of the cantilever and the nuclear magnetization of the sample.

Writing Hamilton's equations, we obtain

$$\dot{q} = \frac{\partial H}{\partial p} = \frac{p}{m} \tag{A.3a}$$

$$\dot{p} = -\frac{\partial H}{\partial q} = -kq - \frac{\partial V^*}{\partial q}, \tag{A.3b}$$

which are easily combined as

$$m\ddot{q} + kq = -\frac{\partial V^*}{\partial q}. \tag{A.4}$$

We need an expression for the interaction energy between the tip and sample $V^*(q,t)$. A suitable expression can be derived from an examination of the interactions of the spins with the cantilever, considered as magnetic dipole moments.

The force exerted on a single magnetic moment $\mathbf{m}_0$ (taken to be the cantilever tip) by N others (taken to be sample spins) is (Griffiths, 1999, 258)

$$\mathbf{F} = \nabla\left(\mathbf{m}_0 \cdot \mathbf{B}\right) \tag{A.5}$$

where $\mathbf{B}$ is the field generated by the N sample spins. By the form of this equation, we easily recognize the interaction Hamiltonian as the negative of that of which the gradient is taken,

$$H_{\text{int}} = -\mathbf{m}_0 \cdot \mathbf{B}. \tag{A.6}$$

The magnetic field at the magnetic tip generated by a dipole $\mathbf{m}_i$ at position $\mathbf{r}_i$ relative to the magnetic tip is (Griffiths, 1999, 246)

$$\mathbf{B} = \frac{\mu_0}{4\pi}\sum_{i=1}^{N}\frac{3\left(\mathbf{m}_i \cdot \hat{\mathbf{r}}_i\right)\hat{\mathbf{r}}_i - \mathbf{m}_i}{r_i^3} \tag{A.7}$$

$$= -\frac{\mu_0}{4\pi}\sum_{i=1}^{N}\frac{\mathbf{m}_i}{r_i^3} - \frac{3\left(\mathbf{m}_i \cdot \mathbf{r}_i\right)\mathbf{r}_i}{r_i^5} \tag{A.8}$$

We combine (A.6) and (A.8) to obtain the interaction Hamiltonian[4],

$$H_{\text{int}} = \frac{\mu_0}{4\pi}\sum_{i=1}^{N}\frac{\mathbf{m}_0 \cdot \mathbf{m}_i}{r_i^3} - \frac{3\left(\mathbf{m}_0 \cdot \mathbf{r}_i\right)\left(\mathbf{m}_i \cdot \mathbf{r}_i\right)}{r_i^5}. \tag{A.9}$$

Considering the one-dimensional case in which all moments are considered to be aligned with

---

[3] Note that $k = m\omega_n^2$, where m is the effective mass of the cantilever and ω_n is the natural angular frequency when the nuclear magnetization is in equilibrium.

[4] This is in accordance with Slichter (Slichter, 1996, 66) who includes the spin-spin interactions in his Hamiltonian.

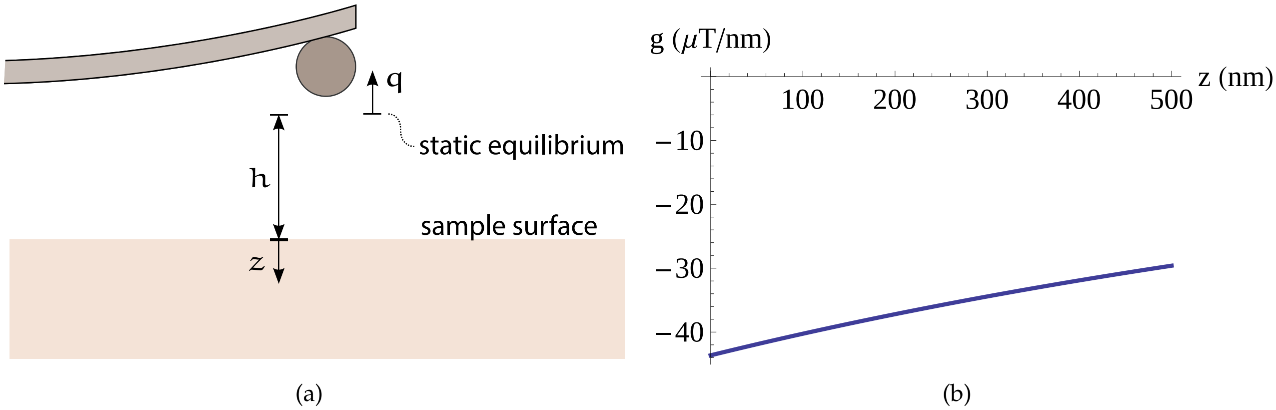

Figure A.7: (a) The coordinate system used for cantilever dynamics and (b) the gradient of B_0 as a function of z, where the origin denotes the location of the resonant slice when the electron-resonant field has angular frequency $2 \times 2\pi$ rad s^{-1}.

this direction,

$$H_{\text{int}} = -\frac{\mu_0}{2\pi} m_0 \sum_{i=1}^{N} \frac{m_i}{r_i^3} \tag{A.10}$$

$$= -\frac{\mu_0}{2\pi} m_0 \int_0^\infty \frac{[\rho_\varepsilon]_2(t,z)}{(q+h+z)^3} A \; dz \tag{A.11}$$

where h locates the sample surface relative to the origin of q, z is the depth into the sample (see Figure A.7), and A is a characteristic area, here taken to be the area of the electron resonant slice. Since we are attempting to gain an understanding of the effect of the interaction between the nuclear spins and the cantilever, we would benefit by extracting q from the integral in (A.11), which can be achieved with a Taylor series expansion of the coefficient of $[\rho_\varepsilon]_2(t,z)$ in the integrand in q about $q = 0$,

$$(q+h+z)^{-3} = (h+z)^{-3} - 3(h+z)^{-4} q + 12(h+z)^{-5} q^2 + \cdots . \tag{A.12}$$

We take only the terms constant, linear, and quadratic in q, since these will be reduced in order in the equation of motion and higher powers can be ignored because q is small. So (A.11) becomes

$$H_{\text{int}} \approxeq -A\frac{\mu_0}{2\pi} m_0 \left(\int_0^\infty \frac{[\rho_\varepsilon]_2(t,z)}{(h+z)^3} \; dz - 3q \int_0^\infty \frac{[\rho_\varepsilon]_2(t,z)}{(h+z)^4} \; dz + 12q^2 \int_0^\infty \frac{[\rho_\varepsilon]_2(t,z)}{(h+z)^5} \; dz \right) \tag{A.13}$$

Choosing this approximation of the Hamiltonian spin-tip interaction to the potential function V^*, we obtain

$$\frac{\partial V^*}{\partial q} = -A\frac{\mu_0}{2\pi} m_0 \left(-3 \int_0^\infty \frac{[\rho_\varepsilon]_2(t,z)}{(h+z)^4} \; dz + 24q \int_0^\infty \frac{[\rho_\varepsilon]_2(t,z)}{(h+z)^5} \; dz \right) \tag{A.14}$$

which enters the equation of motion (A.4) as

$$m\ddot{q} + kq = A\frac{\mu_0}{2\pi}m_0\left(-3\int_0^\infty \frac{[\rho_\varepsilon]_2(t,z)}{(h+z)^4}\,dz + 24q\int_0^\infty \frac{[\rho_\varepsilon]_2(t,z)}{(h+z)^5}\,dz\right) \tag{A.15}$$

or, collecting terms,

$$m\ddot{q} + (k+\delta k)q = f \tag{A.16}$$

where

$$\delta k = -12A\frac{\mu_0}{\pi}m_0\int_0^\infty \frac{[\rho_\varepsilon]_2(t,z)}{(h+z)^5}\,dz \tag{A.17}$$

and

$$f = -A\frac{3\mu_0}{2\pi}m_0\int_0^\infty \frac{[\rho_\varepsilon]_2(t,z)}{(h+z)^4}\,dz. \tag{A.18}$$

We can interpret (A.17) as a shift in natural frequency $\delta\omega_n$. A first order Taylor series expansion of $\delta\omega_n$ in δk about zero is

$$\begin{aligned} \delta\omega_n &= \sqrt{\frac{k+\delta k}{m}} - \sqrt{\frac{k}{m}} && \text{(A.19a)} \\ &\approx \frac{\delta k}{2\sqrt{km}}. && \text{(A.19b)} \end{aligned}$$

Equation A.19 represents the dynamic interaction between the cantilever and sample spins which we seek to measure.

Assuming a standard model of damping on the oscillator, a leading order approximation of the expected phase shift is

$$\delta\phi \approx \frac{2Q}{\omega_n}\delta\omega_n \approx \frac{Q}{k}\delta k. \tag{A.20}$$

This expression can be found by finding a Taylor series expansion about ω_n of the phase between input force and output motion of a damped harmonic oscillator.

A.5 Experimental results

The experimental results presented here[5] are representative of the broader result that, in the parameter space searched, no SMT was observed.

Following the general measurement protocol described above, Run 618 had the specific protocol: (1) a gradient in the electron spin polarization was induced by saturating it with an electron-resonant alternating magnetic field with frequency 2.5 gigahertz in a region of the sample near its surface; (2) after allowing time for SMT, adiabatically inverting the hyperpolarized nuclear-spins with a nuclear-resonant adiabatic inversion pulse (varying from 4.3 to 4.7 megahertz with

---

[5] A comprehensive report of the data is available online at https://www.dropbox.com/s/gwnnmmhyycm8bh7/experiment_DNP006_DawnThree.pdf (300 pages).

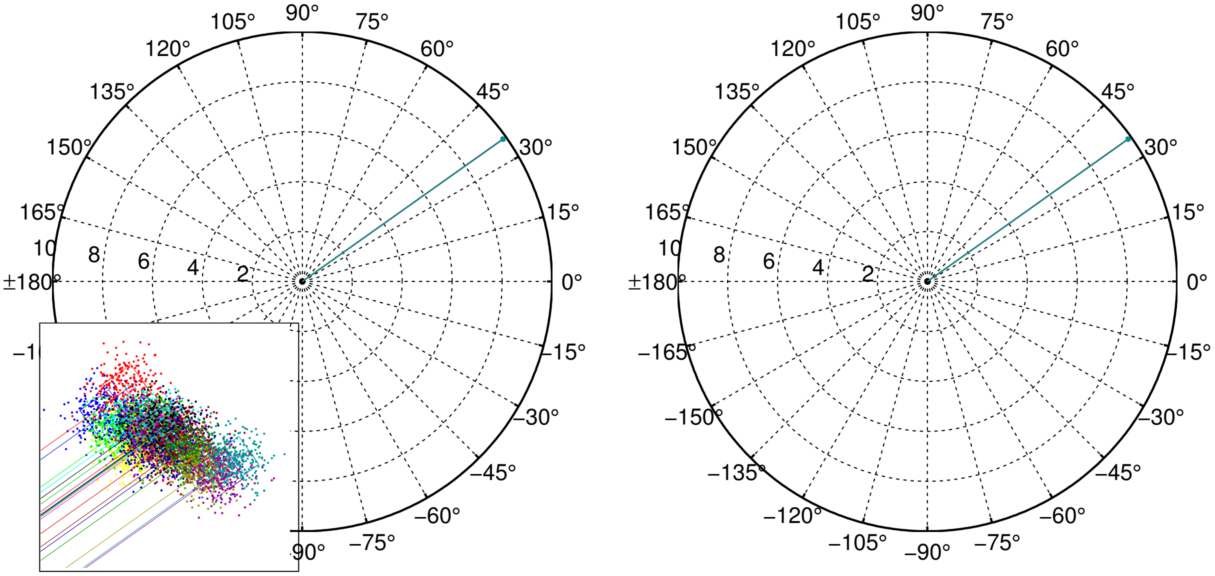

(a)

(b)

Figure A.8: Polar plots of the data from Run 618. (a) A polar plot is shown with magnification inset detailing the data, which is averaged-over 125 one-second intervals, each beginning with a nuclear inversion-pulse, such that the mean one-second time-response is described (implicitly) in the succession of the points of each color. The error boxes represent one standard deviation. The colors correspond to those of Figure A.6. (b) The same data is plotted with a "stretched" phase, such that small differences can be observed.

sweeps of 64 kilohertz) of magnitude approximately 1.25 to 1.35 millitesla; (3) driving the cantilever to oscillations of amplitude 10 nanometers; (4) and measuring the amplitude and phase of the response of the cantilever.

Due to the spatially varying magnetic field, a frequency sweep in the nuclear-resonant alternating magnetic field frequency will correspond to a spatial sweep of the nuclear-resonant resonant slice according to the magnetic resonance condition. For Run 618, the data for which will here be presented, Figure A.6 illustrates the nuclear-resonant sweeps in relation to the stationary electron-resonant slice. Note that this figure can also be used as a legend for the plots that follow it.

The magnitude and phase of the response of the cantilever was recorded for the duration of a nuclear-resonant sweep and for a time considered long-enough for the system to return to equilibrium (one second). One hundred twenty-five repetitions of each measurement were performed. Averaging yielded good estimates of each measurement. The data is presented in Figures A.8 and A.9 as polar plots and variations of magnitude and phase versus time (respectively). The targeted signal was a fast phase-shift (and lesser magnitude-shift) in the response of the cantilever. This was not observed, but a low upper-bound was established for the parameter-

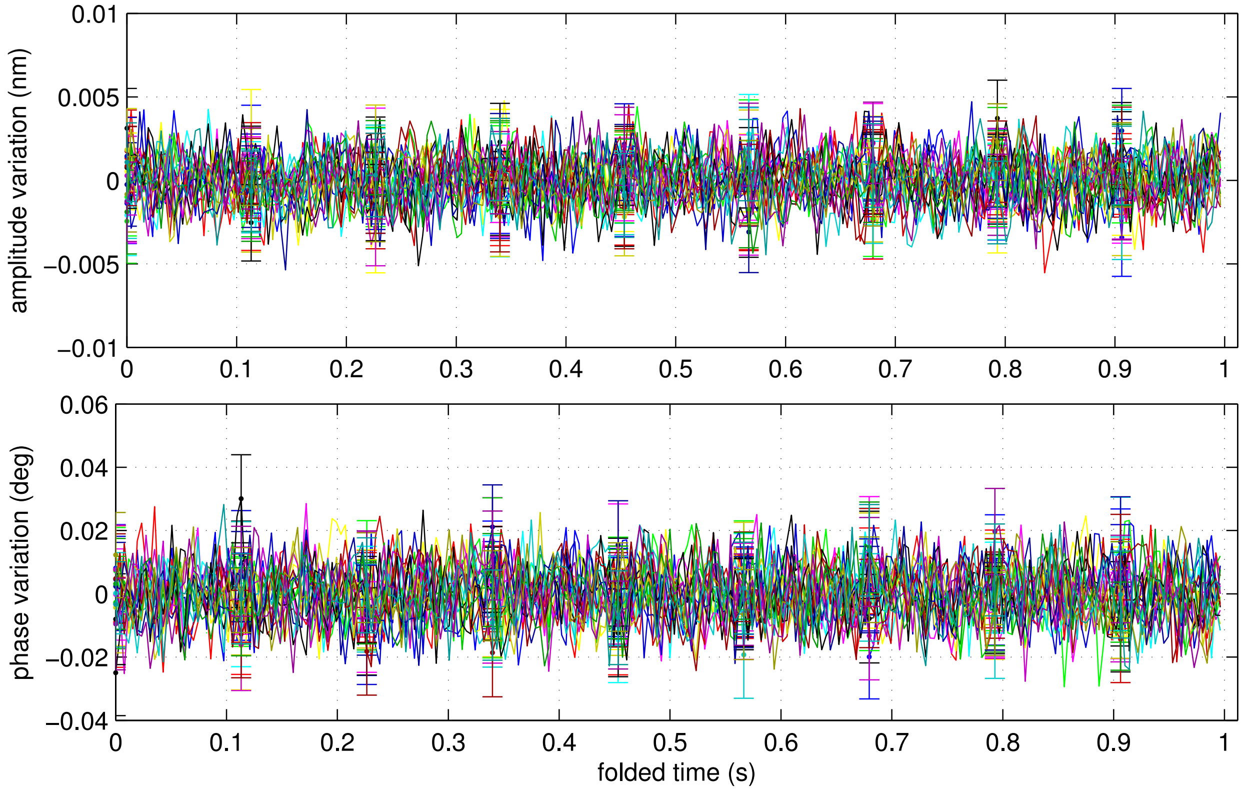

Figure A.9: Variations in amplitude and phase over time of the data from Run 618. With mean subtracted, from each set, and with 125 averages, the data is shown to have very little deviation from its average — that is, no SMT-effects were observed, but a small upper-bound was established.

space explored.

Figure A.8 shows that the measurements were very precise, and that they would have detected even small fractions of a degree of phase-shift (e.g. a tenth of a degree would have been easily distinguished). A slight long-term secular drift was observed in the measurements, as is apparent in the wandering centers of each data-cluster or “dandelion.” This is believed to be inconsequential for these experiments because relatively (very) fast secular variations are the target measurements.

Figure A.9 shows the variations in the magnitude and phase as functions of time. The mean is subtracted from each data-set, such that the long-term secular drift does not affect the representation. The figure shows no significant variation from zero, which confirms the null result. Note, once again, the high-precision of the measurements. Based on early models, this measurement would have detected the magnitudes of signal predicted.

Appendix B

An alternative entropy density function

The entropy density function of Definition 3.4 (two-species local entropy density) is not the only function that meets the criteria of Definition 2.6 (local entropy density) and describes a two-species system. It is a testament to the robustness of the theory that it does not depend significantly on such choices. In this appendix, we present an alternative entropy density function that may be used to derive a similar model to that presented above. However, this function is analytically intractable, whereas the function of Definition 3.4 yields analytically well-behaved mathematical structures.

Definition B.1 (alternative two-species local entropy density)**.** Let Δ_2 and Δ_3 be the temporally invariant volumetric spin densities (spins per unit volume), B be the external spatially varying magnetic field, B_d be the maximum dipole magnetic field,[a] and μ_2 and μ_3 be the magnetic moments of individual spins of each species.[b] Additionally, let the linear forms $\boldsymbol{\Psi}_1, \boldsymbol{\Psi}_2, \boldsymbol{\Psi}_3 \in \mathcal{O}$ be

$$\boldsymbol{\Psi}_1 = \frac{E_1 + B(r)\ E_2 + B(r)\ E_3}{B_d\left(|\mu_2|\Delta_2 + |\mu_3|\Delta_3\right)} \tag{B.1a}$$

$$\boldsymbol{\Psi}_2 = \frac{1}{\mu_2\Delta_2}\ E_2 \tag{B.1b}$$

$$\boldsymbol{\Psi}_3 = \frac{1}{\mu_3\Delta_3}\ E_3 \tag{B.1c}$$

and let the function $\xi : (-1, 1) \to \mathbb{R}$ be

$$\xi(x) = \frac{1}{2}\ln 4 + \frac{1}{2}(x-1)\ln(1-x) - \frac{1}{2}(x+1)\ln(1+x). \tag{B.1d}$$

Then let the local entropy density $s : V^* \to \mathbb{R}$ be defined as

$$s(\boldsymbol{\rho}) = \sum_{i=2}^{n} \frac{\Delta_i}{\Delta_2}\xi \circ \sqrt{\boldsymbol{\Psi}_1(\boldsymbol{\rho})^2 + \boldsymbol{\Psi}_i(\boldsymbol{\rho})^2}. \tag{B.2}$$

---

[a] We use the estimate $B_d = \frac{\mu_0}{2\pi}\left(|\mu_2|\Delta_2 + |\mu_3|\Delta_3\right)$.

[b] For nuclear and electron spin moments, $\mu_2 = \hbar\gamma_n/2$ and $\mu_3 = -\hbar\gamma_e/2$, where $\gamma_n > 0$ and $\gamma_e > 0$ are the nuclear and electron gyromagnetic ratios.

Appendix C

Symbol reference

sym.	description
$*$	Hodge star operator (Lee, 2012, pp 437-8)
α	relative volatility (Equation 4.26)
B	external spatially varying magnetic field
$\overline{B}$	dimensionless ratio (Table 3.2)
B_d	maximum dipole magnetic field (Definition 3.4)
cov	covariance tensor (Definition 2.11)
Δ_i	spins per unit volume of species i (Definition 3.4)
$\overline{\Delta}$	dimensionless ratio (Table 3.2)
d	exterior derivative (Lee, 2012, pp 362-72)
d^*	Hodge codifferential (Lee, 2012, pp 438-9)
dr^α	cotangent bundle basis
∂_x	partial derivative with respect to x
$\partial/\partial r^\alpha$	tangent bundle basis
E^i	standard thermodynamic covector basis (Def. 2.4)
ε_i	standard thermodynamic vector basis (Def. 2.7)
e^i	thermodynamic covector basis (Def. 3.7)
e_i	thermodynamic vector basis (Def. 3.7)
$\hat{\mathfrak{F}}$	Onsager's kinetic coefficients (Definition 2.8)
$\hat{\mathfrak{F}}_{\mathrm{oz}}$	OZ-*ansatz* kinetic coefficients (Definition 2.14)
$\hat{\Gamma}$	transport rate tensor field (Definition 2.13)
Γ_{oz}	OZ transport coefficient (Definition 2.14)
g	spatial metric (Definition 2.2)
$\hat{\mathfrak{G}}$	entropy Hessian (Definition 2.12)
$\mathbf{j}$	spatial transport current (Definition 2.9)

sym.	description
μ_0	magnetic constant
μ_i	magnetic moment of an individual spin of species i
m	dimension of $\mathcal{U}$ (Definition 2.1)
M	basis transformation (Equation 4.22)
n	number of conserved quantities (Definition 2.3)
N	basis transformation (Equation 4.23)
$\circ$	map composition
$\otimes$	tensor product (Lee, 2012, p 306)
$\mathbf{\Omega}$	local thermodynamic potential (Definition 2.7)
$\mathcal{O}^*$	the set of smooth maps from $\mathcal{U} \times \mathbb{R}$ to $\mathbb{R}^n$
$\mathcal{O}$	the dual space of $\mathcal{O}^*$
p	a point on $\mathcal{U}$
P	standard to polarization basis transform (Definition 3.7)
$\mathbf{q}$	globally conserved quantities (Definition 2.3)
$\boldsymbol{\rho}$	local quantity densities (Definition 2.5)
(r^α)	standard spatial coordinate (Remark 2.1)
R	basis transform (Equation 4.20)
$\sharp$	sharp operator (Lee, 2012, pp 341-3)
s	local entropy density (Definition 2.6)
$T\mathcal{U}$	tangent bundle on $\mathcal{U}$
$T_p\mathcal{U}$	tangent space at $p \in \mathcal{U}$
$T^*\mathcal{U}$	cotangent bundle on $\mathcal{U}$
$T_p^*\mathcal{U}$	cotangent space at $p \in \mathcal{U}$
$\mathcal{U}$	spatial manifold (Definition 2.1)
$\xi_i^\uparrow$	fraction of up-spin in tray i (Equation 4.25)
$\xi_i^\downarrow$	fraction of down-spin in tray i (Equation 4.25)